Biogeochemical dynamics in adjacent mesoscale eddies of opposite polarity

Benedetto Barone[1,2*], Matthew J. Church[3*], Mathilde Dugenne[1,2], Nicholas J. Hawco[4,2], Oliver Jahn[5], Angelicque E. White[1,2], Seth G. John[4], Michael J. Follows[5], Edward F. DeLong[1,2], and David M. Karl[1,2]

[*] These authors contributed equally

[1] Daniel K. Inouye Center for Microbial Oceanography: Research and Education, University of Hawai‘i at Mānoa, Honolulu, Hawai‘i, United States of America

[2] Department of Oceanography, University of Hawai‘i at Mānoa, Honolulu, Hawai‘i, United States of America

[3] Flathead Lake Biological Station, University of Montana, Polson, Montana, United States of America

[4] Department of Earth Sciences, University of Southern California, Los Angeles, California, United States of America

[5] Department of Earth, Atmospheric and Planetary Sciences, Massachusetts Institute of Technology, Cambridge, Massachusetts, United States of America

Running title: Biogeochemical dynamics in adjacent eddies

Keywords: Mesoscale eddy; deep chlorophyll maximum; nutrient injection; diapycnal mixing; chemical wake

Correspondence to: B. Barone; benedetto.barone@gmail.com; M. J. Church; matt.church@flbs.umt.edu

Key points

- The steepness of the nutricline in mature mesoscale eddies is an important driver of the variability of pelagic ecosystems
- Differences in eukaryotic phytoplankton communities alter the export of calcium carbonate and opal containing particles across eddies
- Relative changes in oxygen and nutrients linked with displacements of the thermocline are inconsistent with the cycling of organic matter

Abstract

We examined the biogeochemical impact of pairs of mesoscale cyclones and anticyclones in spatial proximity (<200 km apart) in the North Pacific Subtropical Gyre. While previous studies have demonstrated that upwelling associated with the intensification of cyclonic eddies supplies nutrients to the euphotic zone, we find that cyclonic eddies in their mature stage sustain plankton growth by increasing the diapycnal flux of nutrients to the lower portion of the euphotic zone. This increased supply results from enhanced vertical gradients in inorganic nutrients due to erosion of the nutricline that accompanied plankton growth during eddy intensification. From a biological standpoint, increased nutrient flux was linked with expansion of eukaryotic phytoplankton biomass and intensification of the deep chlorophyll maximum layer. This perturbation in the plankton community was associated with increased fluxes of biominerals (opal and calcium carbonate) and isotopically enriched nitrogen in particles exported in the cyclone. The time-integrated effects of thermocline uplifts and depressions were predictable deficits and surpluses of inorganic nutrients and dissolved oxygen in the lower euphotic zone. However, the stoichiometry of changes in oxygen and inorganic nutrients differed from that predicted for production and consumption of phytoplankton biomass, consistent with additional biological processes that decouple changes in oxygen and nutrient concentrations. The dynamics revealed by this study may be a common feature of oligotrophic ecosystems, where mesoscale biogeochemical perturbations are buffered by the deep chlorophyll maximum layer, which limits the ecological impact of eddies in the well-lit, near-surface ocean.

1. Introduction

Subtropical gyres are the dominant circulation features in all major ocean basins (Pedlosky, 1990), enclosing large biomes that cover ~40% of the Earth's surface (McClain et al., 2004). Ecological variability in the subtropical gyres is closely linked to physical variability driven by ocean currents (Mackas et al., 1985), which are most energetic at the mesoscale (10s to 100s of km; Munk 2002) where the circulation forms closed vortices called nonlinear mesoscale eddies (Chelton et al., 2007). A prior study, from a fixed location in the North Pacific Subtropical Gyre (NPSG), revealed eddies were present 30% of the time (Barone et al., 2019). Hence, understanding how mesoscale eddies impact pelagic ecosystem functioning in subtropical gyres is an important step to identify the main drivers of biogeochemical variability in these expansive biomes.

Eddies exert direct influence on plankton biogeochemistry (Falkowski et al., 1991) through vertical oscillations of the thermocline (Wunsch, 1997), with concomitant changes in the vertical distributions of nutrients relative to the upper ocean light field. Cyclonic eddy uplift of the thermocline can enhance the supply of inorganic nutrients to the upper water column, while downward displacement of the thermocline in anticyclonic eddies can move the deep reservoir of inorganic nutrients further away from the sunlit upper ocean (Venrick, 1990; McGillicuddy and Robinson, 1997). The intensification phase of cyclonic eddies is a transient event most often associated with active upwelling, delivering inorganic nutrients to the euphotic zone and supporting phytoplankton production (Sweeney et al., 2003; Rii et al., 2008).

Satellite remote sensing has previously been leveraged to describe the impact of mesoscale eddies on near-surface ocean plankton dynamics by analyzing spatial anomalies in chlorophyll concentrations relative to the eddy field (Chelton et al., 2011; Gaube et al., 2014, Guo et al., 2019). These mesoscale chlorophyll anomalies are caused by different processes including

58 horizontal stirring, vertical motions, and trapping and transport of water parcels, with different
59 processes driving the variability in different oceanic regions (Gaube et al., 2014, Guo et al.,
60 2019). While satellite-based approaches provide valuable insights into physical-biological
61 interactions associated with eddies, they are restricted to the near-surface ocean and do not
62 provide information on dynamics occurring in the deeper regions of the euphotic zone. This is
63 particularly important in stratified ecosystems where the surface mixed layer is shallower than the
64 euphotic zone, and phytoplankton dynamics occurring within vertically distinct layers of the
65 upper ocean can be uncoupled.
66 In this study, we focused on mesoscale eddies in the permanently stratified central NPSG.
67 This ecosystem is characterized by persistently low inorganic nutrients throughout the upper
68 ~100 m, where there is sufficient light to drive net primary production (Karl, 1999). In this
69 environment, phytoplankton communities are vertically segregated (Venrick, 1982; Venrick,
70 1999; Malmstrom et al., 2010), with populations in the near-surface waters distinct from those in
71 the lower portion of the euphotic zone (100-175 m). Low-light adapted phytoplankton
72 assemblages inhabit the deep chlorophyll maximum (DCM), a persistent feature in stratified
73 ocean ecosystems (Li et al., 2011; Malmstrom et al., 2010). In the NPSG, the vertical position of
74 the DCM is defined by time-varying changes in the depth of light penetration (Letelier et al.
75 2004) and it broadly marks the transition between nutrient-limited phytoplankton growth above it
76 and light-limited phytoplankton growth below it (Cullen, 2015). Increased light energy to the
77 lower euphotic zone during the summer months allows vertical expansion of the upper ocean
78 habitat available to phytoplankton, resulting in a downward vertical displacement of the DCM
79 into denser, more nutrient-enriched waters (Letelier al., 2004). In an analogous way, through
80 changes in the depth of isopycnal surfaces across an exponential attenuation in light flux,

mesoscale dynamics structure the vertical positioning of the DCM phytoplankton community, with the DCM forming along colder, denser waters during periods of isopycnal uplift, such as those driven by cyclonic eddies (Falkowski et al., 1991; McGullicuddy et al. 1999; Letelier et al. 2000; Vaillancourt et al. 2003; Kuwahara et al. 2008).

The main objective of this research was to better define the impacts that mesoscale eddies have on the near-surface and DCM plankton communities. To do so, we sampled adjacent eddies with opposite polarity, cyclonic and anticyclonic, in close spatial proximity during two research cruises conducted in 2016 and 2017. Studying adjacent eddies permitted direct comparison of these features without complications due to larger-scale horizontal variability. The eddies sampled as part of these cruises represented extreme mesoscale events for this region (Barone et al. 2019), providing new information on biogeochemical and plankton dynamics associated with strong mesoscale perturbations. The generality of the biogeochemical and ecological responses observed in these strong eddies was subsequently evaluated by leveraging the Eulerian observations of the Hawaii Ocean Time-series (HOT) program and through comparisons with a global ecosystem model.

2. Material and methods

2.1 Identification of eddies

We sampled adjacent eddies of opposite polarity during two oceanographic expeditions: HOE-Legacy 4 (HL4) aboard the R/V *Ka`imikai-O-Kanaloa* (May 9-14, 2016); and MESO-SCOPE aboard the R/V *Kilo Moana* (June 26-July 15, 2017). Eddies were identified as minima (cyclones) and maxima (anticyclones) in sea level anomalies (SLA) based on a combination of all available satellite altimetry products distributed by the Copernicus Marine Environment Monitoring Service (http://marine.copernicus.eu). The SLA products were corrected for

interannual trends and seasonal cycles following procedures recently proposed for the nearby Station ALOHA (Barone et al., 2019), located at 22° 45' N and 158° W; the resulting corrected SLA is henceforth termed SLA_{corr}.

Prior to each cruise, maxima and minima in SLA_{corr} in waters north of the Hawaiian Islands were monitored for several weeks; the selection of eddies to sample for these cruises included consideration of proximity to Station ALOHA (for historical context and logistical considerations), the strength of the adjacent eddies (based on SLA_{corr}), and assessment of time-varying eddy behavior (e.g., strengthening or weakening in SLA_{corr}). Eddy coordinates, age, and amplitude were tracked in time using a simple algorithm: For each daily map of SLA_{corr}, the eddy center was defined as the minimum or maximum of SLA_{corr} in a square with a side of 1.5° centered on the coordinates of the eddy center on the previous day. The amplitude of an eddy was defined as the value of SLA_{corr} at the minimum or maximum. The age of each eddy was defined as the number of days since the time of first detection, which was subjectively assessed as the first day when a minimum or maximum detached from a larger area of positive or negative SLA_{corr}. Similarly, the last day of eddy detection was subjectively defined as the day when a minimum or maximum of SLA_{corr} could no longer be distinguished within a larger region with positive or negative SLA_{corr}.

While we adopted a simplified tracking algorithm to describe eddy life history, eddies are also routinely catalogued and tracked within the mesoscale eddy trajectory atlas (Schlax and Chelton, 2016) distributed by AVISO+ (Archiving, Validation and Interpretation of Satellite Ocean data; doi: 10.24400/527896/a01-2021.001). The four eddies sampled in this study were all reported in the eddy atlas, but the MESO-SCOPE cyclone was considered as a single feature together with a second cyclonic eddy during part of its lifetime. However, the trajectory of the

surface drifters (described in section 2.5) deployed during MESO-SCOPE showed cyclonic circulation around the SLA_{corr} minimum defined as the eddy center in this study, hence it is likely that the two minima which were merged in the eddy atlas represented distinct features.

2.2 Water sampling and profiling instruments

During transit, the hydrographic characteristics were measured using underway conductivity, temperature, and depth (CTD) profilers (underway CTD, Teledyne), while current speed and direction were measured using hull-mounted acoustic doppler current profilers (ADCP, Workhorse 300 kHz, Teledyne). Upper ocean biogeochemical properties were characterized using a rosette system mounting 10 L Niskin® sampling bottles and profiling instruments including a CTD sensor (Sea-Bird 9/11 plus), a chlorophyll fluorometer (Seapoint SCF), a polarographic oxygen (O_2) sensor (SBE 43, Sea-Bird), and a transmissometer (c-star, Sea-Bird). In situ chlorophyll fluorescence was calibrated using a linear regression against the concentration of chloropigments (comprised mostly of monovinyl and divinyl forms of chlorophyll *a* and *b*), measured fluorometrically. Similarly, the O_2 sensor was calibrated from a linear regression of dissolved O_2 concentrations determined at discrete depths measured using a Winkler titration system (see below). Beam attenuation measurements that exceeded three standard deviations from the mean based on 20 m vertical bins were removed in order to exclude observations presumably due to rare, large particles. Furthermore, to account for variations in sensor background values among deployments, the minimum value measured between 350-400 m was subtracted from each beam attenuation profile (this approach assumes that particle scattering is constant in the 350-400 m layer).

Light flux at discrete depths was calculated as the product of the daily-integrated downwelling cosine PAR irradiance above the sea surface measured with a shipboard sensor (LI-

COR LI-190), and the fraction of downwelling PAR penetrating at depth measured using a free-falling optical profiler (Sea-Bird Hyperpro II).

2.3 Eddy transects

Physical and biogeochemical characterizations of each of the eddy couples were obtained by shipboard sampling along an approximately linear transect crossing both eddy centers (Figure 1a,b). An initial physical characterization was obtained while transiting using the ADCP and the underway CTD. Biogeochemical observations were obtained at a lower horizontal resolution along transects including 5 stations in 2016 and 11 stations in 2017, where measurements were collected using the CTD rosette sampler. For these stations, hydrography and other profiling sensor observations were measured using the instruments attached to the CTD rosette.

During HL4 (in 2016) there was a failure of the conductivity sensor that prevented an accurate determination of salinity; hence, for this cruise only temperature observations from the underway CTD are presented. Since this problem only impacted the underway instrument, measurements of salinity and potential density associated with the biogeochemical observations were still available from CTD measurements collected when the ship was stationary.

2.4 High vertical resolution sampling

In the four eddy centers, the layer surrounding the DCM was characterized using high vertical resolution sampling (approximately 5 m vertical intervals) at 15 discrete depths around the DCM (6 depths above the DCM, 8 depths below the DCM, in addition to the DCM). The DCM was identified during each CTD deployment as the depth of the fluorescence maximum (ranging from 96 to 151 m). This sampling was consistently done at 0700 local time to account for possible diel variability in biogeochemical properties. The objective of this high vertical

resolution sampling was to characterize changes in water chemistry and plankton community composition above, within, and below the DCM.

2.5 MESO-SCOPE Lagrangian sampling

During the 2017 expedition, we extended our observations through Lagrangian sampling of the eddy centers using surface velocity program (SVP, Pacific Gyre) drifters with a drogue centered at 15 m depth. Initially, eddy centers were identified using shipboard ADCP measurements of upper ocean currents and underway hydrographic characterization conducted while transiting across the eddies. Using this information, a SVP drifter was deployed in the predicted center of each eddy (lowest current velocity and deepest or shallowest isopycnal depth). These drifters advanced in arcs consistent with the geostrophic flow. A second SVP drifter was then deployed near the center of the drift arcs to decrease the distance from the eddy center. The research vessel followed these secondary drifters conducting high-temporal resolution Lagrangian sampling over 3-4 days. The distance between the drifter and the ship at the Lagrangian sampling stations averaged 1.1±0.8 (standard deviation) km, with a maximum distance of 4.1 km.

2.6 Biogeochemical sample collection and analyses

The analytical methods used for assessing upper ocean biogeochemical properties, including concentrations of dissolved O_2, chlorophyll, dissolved and particulate nutrients, and fluxes of particulate matter derived from sediment trap collections followed protocols utilized by the HOT program (http://hahana.soest.hawaii.edu/hot/methods/results.html). Briefly, concentrations of chlorophyll were determined from filtered seawater samples (25 mm diameter glass fiber filters; Whatman GF/F, nominal porosity 0.7 μm). Concentrations of chlorophyll *a* and phaeopigments were measured fluorometrically on a Turner Designs Model 10-AU fluorometer

196 (Strickland and Parsons, 1972). Note that, in this environment, fluorescence from chlorophyll *b* is
197 a major contributor to "phaeopigment" determinations (Karl et al., 2001). Seawater for
198 subsequent determinations of particulate carbon (PC) and nitrogen (PN) was prefiltered through
199 202 µm Nitex © mesh screen, followed by positive pressure filtration onto precombusted 25 mm
200 diameter glass fiber filters (Whatman GF/F). Filters were frozen at -20°C until analysis in the
201 laboratory. PC and PN concentrations were determined using an Exeter Analytical CE-440 CHN
202 elemental analyzer (Exeter Analytical, UK) as described in Grabowski et al. (2019).
203 Samples for the determination of dissolved O_2 were collected into borosilicate flasks, fixed
204 with manganous chloride and alkaline iodide, acidified, and dissolved O_2 concentrations were
205 determined by titration with thiosulfate (Carpenter, 1965). Water samples for subsequent
206 determinations of the sum of nitrate plus nitrite (hereafter N + N) and soluble reactive
207 phosphorus (herein termed phosphate, PO_4^{3-}) concentrations were collected in acid-washed
208 polyethylene bottles and stored frozen until analyzed (Dore et al., 1996) using a Bran Luebbe
209 Autoanalyzer III. For most samples where N+ N concentrations were below 100 nM,
210 concentrations were determined using a chemiluminescent method (Foreman et al. 2016).
211 Iron (Fe) was sampled using a trace metal clean rosette and analyzed by inductively
212 coupled plasma mass spectrometry after preconcentration by an automated SeaFAST system
213 (Elemental Scientific; see Hawco et al., companion submission, for full description).
214 *2.7 Calculation of isopycnal anomalies and nutrient gradients*
215 We calculated isopycnal concentration anomalies for inorganic nutrients and O_2 for both
216 HL4 and MESO-SCOPE cruises to illustrate biogeochemical changes driven by past physical-
217 biological processes in mesoscale eddies. These anomalies represent the concentrations of N+N,
218 PO_4^{3-}, and O_2 measured along an isopycnal surface minus the cruise-averaged concentrations

measured on the same isopycnal. Computing anomalies in this manner assumes similar initial concentrations of nutrients and O_2 for a given isopycnal surface, and that mesoscale physical-biological linkages drive variations in these properties.

Vertical gradients in inorganic nutrient concentrations were calculated as the slope of Model I linear regressions of nutrient concentration versus depth at depths between 10 meters above the DCM and down to 90 m below the DCM from individual nutrient profiles collected during HL4 and MESO-SCOPE.

Isopycnal nutrient anomalies and vertical nutrient gradients were compared to near-monthly Eulerian observations conducted by the HOT program at Station ALOHA. These HOT program observations (1988-2020) were used to examine the relationships between SLA_{corr} and the O_2 and inorganic nutrient anomalies along the 24.5 kg m^{-3} isopycnal surface (henceforth we refer to an isopycnal surface based on its potential density anomaly, which is the potential density - 1000 kg m^{-3}). For these analyses, we eliminated potential seasonal variability in O_2 and inorganic nutrient concentrations by subtracting the monthly mean isopycnal concentrations of these properties. When comparing these anomalies with those observed during the HL4 and MESO-SCOPE cruises, for consistency we subtracted the HOT monthly mean concentration also from the isopycnal anomalies calculated on the eddy transects.

The calculation of vertical nutrient gradients on HOT observations followed the same procedure described for HL4 and MESO-SCOPE. Vertical profiles where less than 3 measurements existed in the vertical layer around the DCM were discarded for these analyses.

2.8 Plankton abundance and biomass

Abundances of picocyanobacteria (*Prochlorococcus* and *Synechococcus*) and pigmented eukaryotes (pico- and nanoplankton), together with non-pigmented picoplankton (hereafter

heterotrophic bacteria), were determined by flow cytometry. For these analyses, seawater was collected in 2 mL cryovials, fixed with microscopy-grade paraformaldehyde (0.24% vol/vol final concentration), stored in the dark for 15 min, flash frozen in liquid nitrogen, and stored at -80 °C. Plankton were enumerated with an Influx (Cytopeia) flow cytometer, with pigmented cells distinguished based on their scattering and fluorescence characteristics using two excitation lasers (457 and 488 nm). The abundance of non-pigmented picoplankton (herein defined as heterotrophic bacteria) was determined by staining cells with SYBR Green I DNA and subtracting the contributions from *Prochlorococcus*.

The carbon biomass of larger (4-100 μm) eukaryotic phytoplankton was estimated by automated imaging flow cytometry (Imaging FlowCytobot [IFCb], McLane) over the course of the Lagrangian sampling in 2017. In both eddy centers, daily discrete samples were collected every 4 hours (n=6 at each depth) at 15 m and at the DCM from Niskin® bottles mounted on the CTD rosette. Analyses were carried out within 2 hours of collection to ensure that cells were not deteriorating since samples were not preserved. The IFCb detects individual particles via laser-induced fluorescence and light scattering used to trigger image acquisition of all particles in successive ~5 mL samples.

A training set was used to classify the images to the genus level based on morphological traits, as described in Dugenne et al. (2020). The output of the random forest classifier (Sosik and Olson, 2007) was manually corrected to provide accurate estimates of cell size distribution and concentration for individual genera. For this study, we selected phytoplankton genera, then computed carbon biomass based on a biovolume-to-C quota using class-specific regression coefficients (Menden-Deuer and Lessard, 2000). Standard errors associated with the intercept and

slope of the biovolume-to-C regressions result in a ±20% uncertainty in larger phytoplankton biomass.

2.9 Quantification of particle export

During the MESO-SCOPE cruise, 12 free-drifting sediment trap arrays were deployed along a line connecting the eddy centers (at approximately 18 km spacing) to examine the downward flux of sinking particulate material. Each surface-tethered array included 12 individual particle interceptor trap collector tubes (Knauer et al. 1979). Traps were deployed at 150 m for 10 to 13 days, passively collecting sinking particles. The sediment traps were prepared and processed following HOT program methods (Karl et al. 1996). Trap samples were processed and analyzed for total mass, PC, PN, particulate phosphorus (PPO_4^{3-}), particulate silica (PSi), particulate inorganic carbon (PIC; i.e., calcium carbonate), and stable nitrogen isotope composition in particles (δ^{15}N-PN). From the 12 individual collector tubes, 6 were processed for subsequent measurements of PC, PN, δ^{15}N-PN; 3 were processed for PPO_4^{3-}; and the remaining 3 traps were split and processed for PIC, PSi, and total mass flux. Prior to filtration, trap contents were screened through a 335-μm Nitex mesh to remove any mesozooplankton (swimmers) that are not part of the passive flux of particles. Collection tubes for subsequent analyses of PC and PN were filtered onto 25 mm diameter combusted glass fiber filters, while samples for PPO_4^{3-} analyses were filtered onto combusted, acid-washed glass fiber filters. Samples for PSi and total mass were filtered onto 47 mm diameter, 0.8 μm pore size polycarbonate filters, while PIC samples were filtered onto 25 mm diameter, 0.2 μm pore size polycarbonate filters. All filters were frozen until subsequent analyses. Filters for PC, PN, and δ^{15}N-PN were analyzed on a high-temperature elemental analyzer (Carla Erba NC 2500) coupled to a Finnigan MAT DeltaS mass spectrometer. Filters for total mass were analyzed as described in Karl et al. (1996). Filters for

PIC determinations were placed in gas-tight vials, fumed with phosphoric acid, and the CO_2 evolved in the headspace quantified by infrared absorption (Grabowski et al., 2019). PSi analyses followed the NaOH digestion method for biogenic silica described in Brzezinski and Nelson (1989). Particulate organic carbon (POC) flux was calculated as the difference between PC and PIC.

2.10 Numerical simulation of physical-biological dynamics at Station ALOHA

We examined the relationships between nutrients, phytoplankton biomass, and SLA_{corr} in a global simulation using the Massachusetts Institute of Technology General Circulation Model (MITgcm; Marshall et al., 1997) and associated biogeochemical and ecological components as detailed by Dutkiewicz et al. (2015) but with increased resolution in phytoplankton diversity. The eddy-permitting physical simulation has an effective resolution of 1/6° and horizontal grid of ~18 km (ECCO2; http://ecco2.jpl.nasas.gov/; Menemenlis et al., 2008) which, at subtropical latitudes, resolves mesoscale but not sub-mesoscale features. Briefly, the biogeochemical model resolves cycles of carbon, phosphorus, nitrogen, silica, iron, and oxygen with inorganic, living, dissolved and particulate organic phases. The configuration examined here resolves 35 phytoplankton types spanning several size classes within each of five broad functional classes (diatoms, coccolithophorids, mixotrophs, nitrogen fixers, and pico-phytoplankton). Sixteen size-differentiated types of zooplankton are resolved, but the population of heterotrophic decomposers is implicit (Dutkiewicz et al, 2015). Physical and biogeochemical model codes are available at http://mitgcm.org and https://github.com/darwinproject/darwin3 respectively. Selected simulation results are available at http://simonscmap.org (search term “Darwin”).

For this study, we extracted the simulation results at Station ALOHA with a temporal resolution of 3 days and for a period of 23 years. We computed SLA_{corr} and dN/dz using the same

methods adopted for field observations. The biomass of eukaryotic phytoplankton was obtained by summing the biomass of all eukaryotic phytoplankton types, and the concentration of N+N was obtained as the sum of NO_3^- and NO_2^-, which are represented separately in the model.

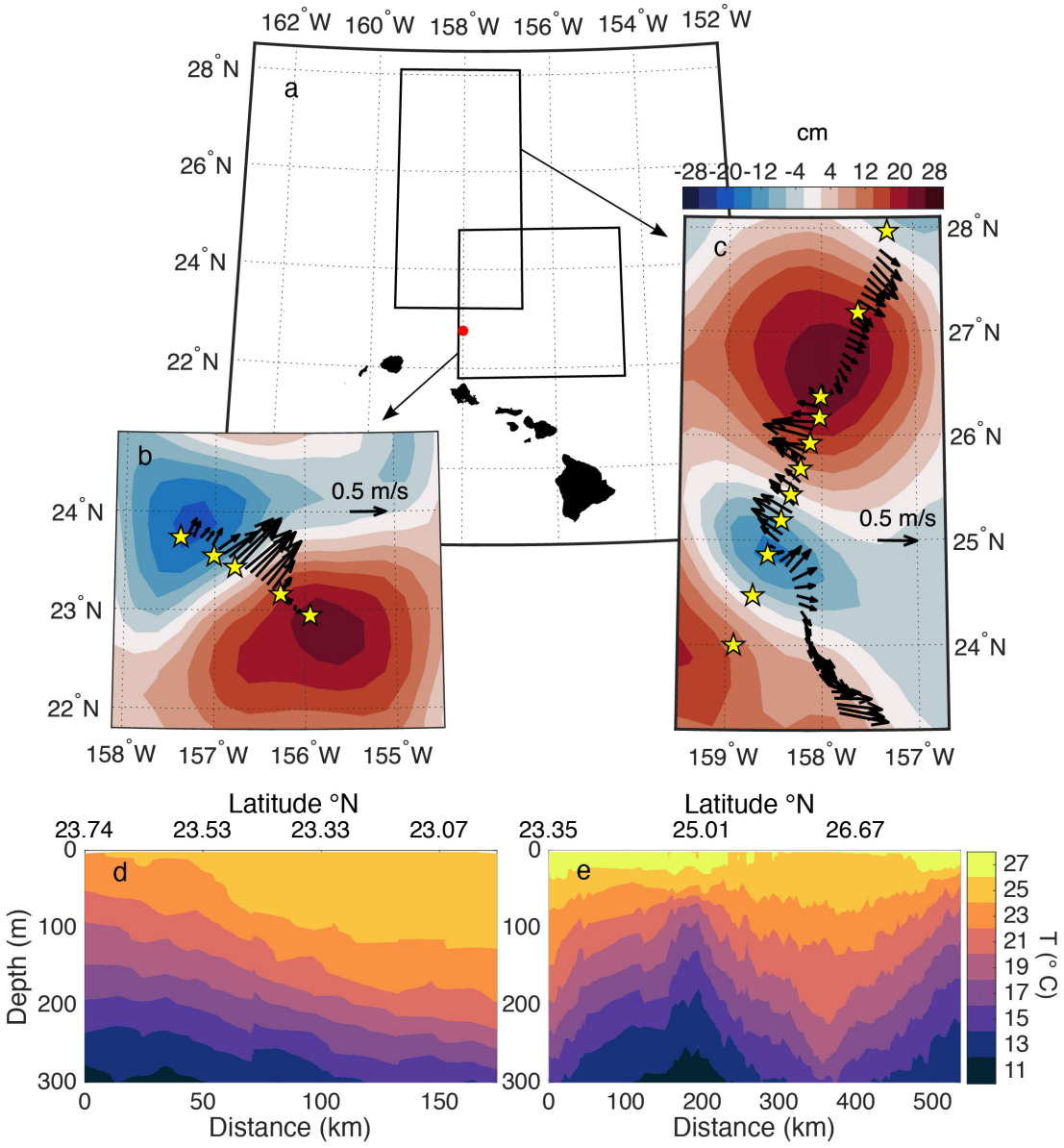

Figure 1: Sampling across adjacent mesoscale eddies during the two expeditions described in this study. The ocean near the Hawaiian archipelago is depicted in a) with black boxes representing the regions sampled during HL4 and MESO-SCOPE, and the red circle representing the position of Station ALOHA. Contours of sea level anomaly are depicted in b) during HL4 (11 May 2016), and c) MESO-SCOPE (28 June 2017). Arrows depict the average current

velocity and direction measured from the research vessel with an acoustic doppler current profiler in the 11-61 m depth layer; yellow stars depict the sampling stations along a transect where water samples were collected from the ship. Temperature contours along the transects are shown in d) for HL4, and e) for MESO-SCOPE. Data from 2016 include both shipboard measurements and measurements collected with an underway profiling CTD system. Data from 2017 include only measurements collected with an underway CTD.

3. Results

3.1 *Transects across adjacent eddies*

The hydrographic and dynamic structure of the sampled eddies was consistent with expectations based on eddy polarity: cyclonic eddies were characterized by an uplifted thermocline and surface currents organized in a counterclockwise circulation, while anticyclones demonstrated deeper thermoclines and clockwise surface current circulation (Figure 1). In both cruises, surface currents were strongest along the frontal boundaries separating the adjacent eddies. During the HL4 cruise, frontal currents reached a maximum velocity of 0.85 m s^{-1} in the 11-61 m layer; during the MESO-SCOPE cruise in 2017 frontal currents reached a maximum velocity of 0.60 m s^{-1}. High horizontal resolution underway CTD profiles conducted during HL4 revealed the depth of the 19°C isotherm varied from 120 m in the cyclone center to 244 m in the anticyclone center (Figure 1d), while this isotherm varied between 79 m in the cyclone center to 255 m in the anticyclone center during MESO-SCOPE (Figure 1e). Similarly, the vertical position of isopycnal surfaces varied with eddy polarity. For example, during the HL4 cruise in 2016, the depth of the 25 kg m^{-3} isopycnal surface (typically occurring near the base of the DCM at Station ALOHA) deepened from 112 m near the cyclone center to 243 m near the anticyclone center (Figure 2), while this isopycnal varied from 84 m near the cyclone center to 220 m near the anticyclone center during the MESO-SCOPE cruise (Figure 2). This isopycnal was shallowest (80 m) in the northernmost station of the MESO-SCOPE cruise transect, reflecting the low SLA

observed at this station, together with shallowing of isopycnals towards the northern edge of the NPSG.

Both of the cyclones and anticyclones sampled as part of this study represented extreme mesoscale events relative to historical Eulerian observations of SLA_{corr} at Station ALOHA (Figure 2). SLA_{corr} in the cyclone and anticyclone eddy centers averaged -18.4 cm and 23.8 cm during HL4 and -14.7 cm and 24.0 cm during MESO-SCOPE, respectively. In both cases, these SLA_{corr} values were more than two standard deviations different from the mean SLA_{corr} measured at Station ALOHA between 1993 and 2018 (Figure 2a,b).

The vertical position of the DCM also varied consistently with eddy polarity, with cyclones characterized by shallower DCM, but more intense chlorophyll fluorescence relative to anticyclones (Figure 2c,d). Moreover, during both cruises, but particularly during MESO-SCOPE, concentrations of dissolved O_2 in the cyclones peaked at depths shallower than the DCM, with O_2 concentrations greatest near the top of the 24.5 kg m^{-3} isopycnal in the cyclones, despite the DCM occurring closer to the 25 kg m^{-3} isopycnal (Figure 2e,f). Concentrations of O_2 along the 24.5 kg m^{-3} isopycnal were greatest in the cyclone sampled during the MESO-SCOPE cruise, peaking at 242.0 mmol m^{-3} and decreasing to 220.9 mmol m^{-3} in the center of the anticyclone (Figure 2). O_2 concentrations measured across the eddies as part of HL4 demonstrated similar patterns, with a peak concentration of 232.7 mmol m^{-3} just below the 24.5 kg m^{-3} isopycnal in the cyclone and decreasing to a maximum 218.8 mmol m^{-3} in the center of the anticyclone (Figure 2).

The observed eddy-dependent vertical changes in isopycnal surfaces resulted in displacement of inorganic nutrient concentrations, with upward displacement of N+N concentrations below the DCM in cyclones, and downward displacement of isopycnals in

anticyclones reducing concentrations of N+N throughout the upper 200 m (Figure 2g,h). N+N concentrations along the 24.5 kg m^{-3} were elevated in the anticyclones, ranging 0.976 and 0.026 mmol m^{-3} during HL4 and MESO-SCOPE, respectively, with lower concentrations in both cyclones (< 0.003 mmol m^{-3}; Figure 2). Along the 25 kg m^{-3} isopycnal, concentrations of N+N ranged between 0.002 and 2.975 mmol N m^{-3} during MESO-SCOPE, and between 3.584 and 0.875 mmol N m^{-3} during HL4, across all stations.

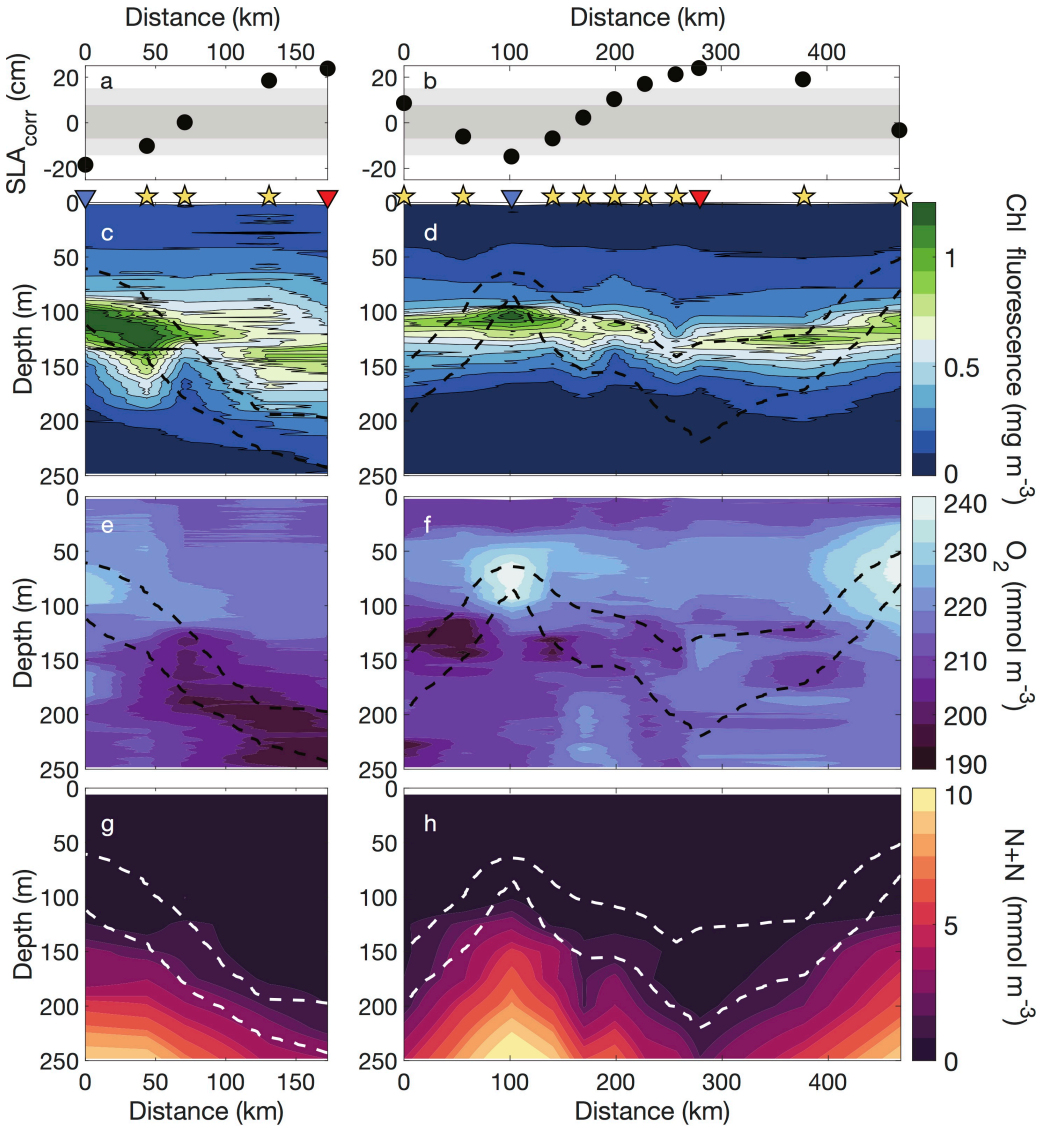

Figure 2: Biogeochemical characteristics along two transects between the couple of adjacent eddies sampled during HL4 in 2016 (panels a,c,e,g) and MESO-SCOPE in 2017 (panels b,d,f,h). a,b) SLA_{corr} at stations sampled during transects across adjacent eddies (black symbols). Shaded areas represent variability in SLA_{corr} at Station ALOHA

between 1993 and 2018, with dark grey shading depicting ±1 standard deviation of the mean and light grey shading depicting ±2 standard deviations from the time-averaged SLA_{corr} value; c,d) Chlorophyll (Chl) fluorescence (e,f), dissolved O_2 concentrations (g,h), and concentrations of N+N during adjacent eddy sampling transects. Dashed lines depict the depth of isopycnal surfaces with potential density anomaly of 24.5 kg m^{-3} (shallower surface), and 25 kg m^{-3} (deeper surface). Symbols on the top panels depict the position of the sampling stations along the transects, with blue and red triangles depicting the stations closest to the cyclone and the anticyclone centers, respectively.

3.2 Isopycnal anomalies of O_2 and inorganic nutrients

Depth-dependent oscillations in the thermocline appear to underlie much of the variability associated with concentrations of inorganic nutrients and dissolved O_2 (Fig. 2g,h). However, analyses of these properties along isopycnal surfaces revealed more subtle dynamics. For both cruises, robust anomalies for both O_2 and inorganic nutrients were observed along isopycnal surfaces located at depths surrounding the DCM. The isopycnal anomalies in cyclonic eddies were consistently positive for O_2 (Figure 3a,b) and consistently negative for N+N and PO_4^{3-} (Figure 3c-f), indicative of prior net phytoplankton production. Anomalies associated with anticyclones demonstrated less robust mesoscale variation: for example, during the HL4 anticyclone anomalies associated with N+N, PO_4^{3-}, and O_2 near the DCM had the opposite sign than those measured in the cyclone, while during MESO-SCOPE inorganic nutrient anomalies near the DCM had the same sign in both the cyclone and anticyclone (Figure 3).

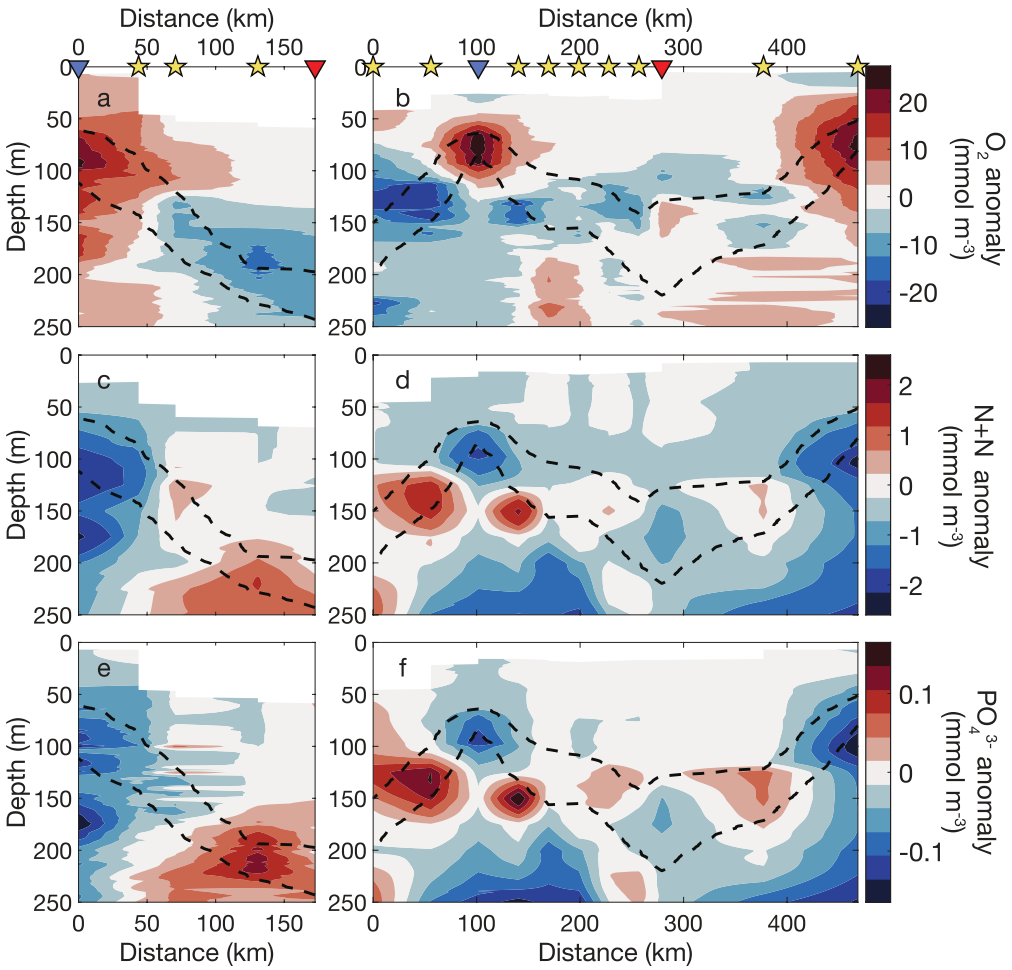

397

398 **Figure 3:** Concentration anomalies of O_2 (a,b), N+N (c,d), and PO_4^{3-} (e,f) with respect to the mean isopycnal
399 concentration measured during sampling transects of adjacent eddies during HL4 (a,c,e) and MESO-SCOPE (b,d,f).
400 Dashed lines depict the depth of potential density anomaly isopycnal surfaces of 24.5 kg m^{-3} (shallower surface), and
401 25 kg m^{-3} (deeper surface). Symbols on the top panels depict the position of the sampling stations along the transect,
402 with blue and red triangles depicting the stations closest to the cyclone and the anticyclone centers, respectively.

403 To assess the generality of mesoscale variability in biogeochemistry along isopycnal
404 surfaces located near the depth of the DCM, we evaluated relationships between SLA_{corr} and both
405 O_2 and inorganic nutrient anomalies along the 24.5 kg m^{-3} surface using historical HOT program
406 measurements (Figure 4). These analyses revealed consistent patterns in both the HOT program
407 observations and the eddy transects. In particular, the seasonally detrended O_2 concentration
408 anomalies decreased with increasing SLA_{corr}, while the de-seasoned concentration anomalies of

409 both N+N and PO_4^{3-} increased with SLA_{corr} (Figure 4). The consistency in concentrations of O_2
410 and inorganic nutrients to variations in SLA_{corr} along this isopycnal surface suggests the patterns
411 we observed are not specific to strong mesoscale eddies, but rather are more generally reflective
412 of the full range of mesoscale motions observed in the region near Station ALOHA. Slopes of the
413 isopycnal concentration anomalies versus SLA_{corr} (Model II geometric mean regression) were -
414 1.07 ± 0.07 mmol O_2 m^{-3} cm^{-1}, 0.102 ± 0.008 mmol N+N m^{-3} cm^{-1} and 0.00860 ± 0.00067 mmol
415 PO_4^{3-} m^{-3} cm^{-1}. The resulting ratios of these slopes were -10.49 (mol O_2 : mol N), -124.4 (mol O_2
416 : mol P), and 11.86 (mol N : mol P). SLA_{corr} explained less of the variability in the inorganic
417 nutrient concentration anomalies than O_2 concentration anomalies (correlation coefficients values
418 for O_2, N+N, and PO_4^{3-} were -0.49, 0.21, and 0.23, respectively, with all $p<0.001$), and this is
419 particularly noteworthy for N+N at low values of SLA_{corr} (i.e., when SLA_{corr} decreases below -10
420 cm, such as would occur with relatively strong cyclonic eddies). Potential Fe limitation of DCM
421 plankton production was also investigated during the MESO-SCOPE cruise and results from that
422 study are described elsewhere (Hawco et al., companion submission). Briefly, dissolved Fe was
423 depleted in the lower euphotic zone of the cyclone , averaging 73 nmol m^{-3} at a potential density
424 of ~25.16 kg m^{-3}, the same isopycnal where we measured the maximum cyclonic deficit of N+N
425 and PO_4^{3-}. In this layer, the cyclone had 110 nmol m^{-3} less Fe than the anticyclone as compared
426 with a 1.80 mmol m^{-3} and 0.11 mmol m^{-3} decreases in N+N and PO_4^{3-}, respectively. Lower
427 dissolved Fe at 25.16 kg m^{-3} in the cyclonic eddy is consistent with biological Fe uptake by
428 phytoplankton.

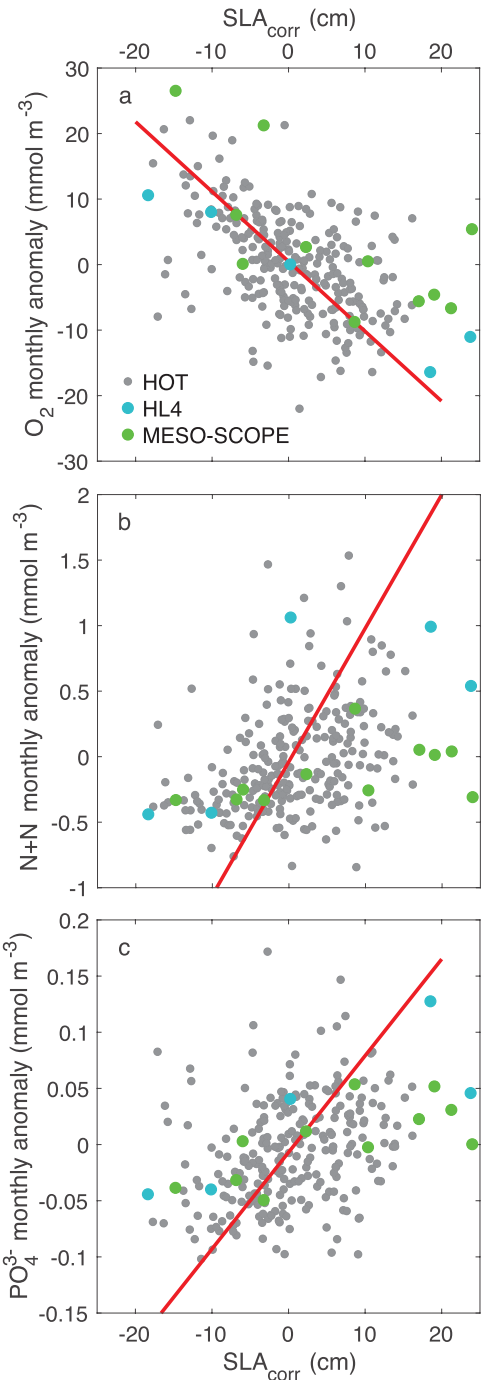

Figure 4: Monthly isopycnal anomalies of the concentrations of O_2 (a), N+N (b), and PO_4^{3-} (c) versus SLA_{corr} from HOT program measurements (gray symbols), the HL4 eddy transect (blue symbols), and the MESO-SCOPE eddy transect (green symbols) along the 24.5 kg m-3 density surface. Red lines depict the Model II geometric mean regression of HOT observations. Note that for visual clarity the y-axes exclude three observations with high concentration anomalies of N+N (2.4, 4.4, and 8.2 mmol m^{-3} corresponding to SLA_{corr} of 8.4, -4.7, and 1.4 cm, respectively) and two observations with high concentration anomalies of PO_4^{3-} (0.28 and 0.56 mmol m^{-3} corresponding to SLA_{corr} of -4.7, and 1.4 cm, respectively).

The isopycnal anomalies of O_2 and inorganic nutrients vary inversely due to primary production and mineralization, which produce O_2 and consume inorganic nutrients (or vice versa) in proportions that are relatively invariant across ocean basin scales (Redfield, 1958; Anderson and Sarmiento, 1994). To assess if the isopycnal variations of O_2 and inorganic nutrients in mesoscale eddies were consistent with the stoichiometry of the production and consumption of organic matter, we calculated the excess O_2 anomaly as follows:

isopycnal anomaly of $(O_2 - O_{2\ solubility}) + 10.5 \times$ isopycnal anomaly of $(NO_3^- + NO_2^-)$

where 10.5 represents the moles of O_2 produced when 1 mole of $NO_3^- + NO_2^-$ is consumed for the synthesis of new organic matter, or the inverse for its consumption (Anderson, 1995; Johnson et al., 2010). For this analysis, we also subtracted O_2 solubility to avoid misinterpreting variations caused by changes in hydrography along the eddy transects. The excess O_2 anomaly was positive in both cyclone centers in a vertical layer located just above the DCM and approximately between 50 and 100 m (Figure 5a). In this layer, the excess O_2 anomaly reached values above 10 mmol m^{-3} in cyclones, while it was close to 0 or negative in both anticyclones (Figure 5). The excess O_2 anomaly was predominantly negative below 100 m in all four eddy centers (Figure 5), indicating that the O_2 concentration in these eddy centers was lower than expected assuming the water started with the average isopycnal concentrations measured along the transect and was later modified assuming fixed 10.5 O_2:N stoichiometry (Anderson, 1995).

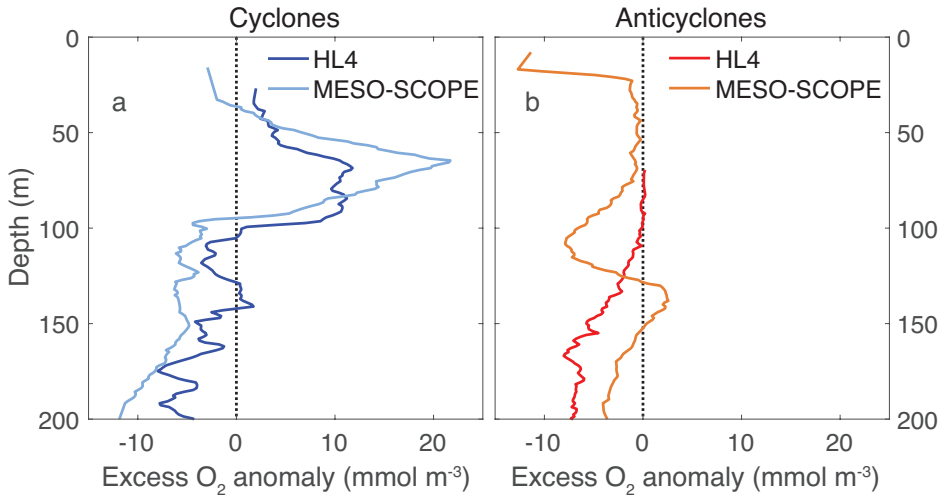

Figure 5: Excess O_2 anomaly in cyclones (a) and anticyclones (b). Excess O_2 anomaly reflects the surplus of O_2 with respect to the concentration expected if starting from the average isopycnal concentrations of O_2 and $NO_3^- + NO_2^-$ along the transects and assuming that they are modified following a fixed -10.5 O_2:N stoichiometry.

3.3 Vertical gradients and mixing estimates at the top of the nutricline

We calculated how mesoscale motions influenced vertical gradients in N+N and PO_4^{3-} based on the slopes of nutrient concentration versus depth relationships calculated from the individual nutrient profiles. Upward displacement of the nutricline associated with cyclonic eddies resulted in vertical gradients in N+N that were 1.8 to 9.2 times greater near the center of the cyclones than in the anticyclones (Figure 6a,b). Similarly, vertical gradients in PO_4^{3-} were 1.8 to 10.8 times greater near the center of the cyclones than in the anticyclones (Figure 6c,d). During both HL4 and MESO-SCOPE cruises, the maximum and minimum vertical gradients were observed at stations close to the centers of the cyclone and of the anticyclone, respectively (Figure 6a,c).

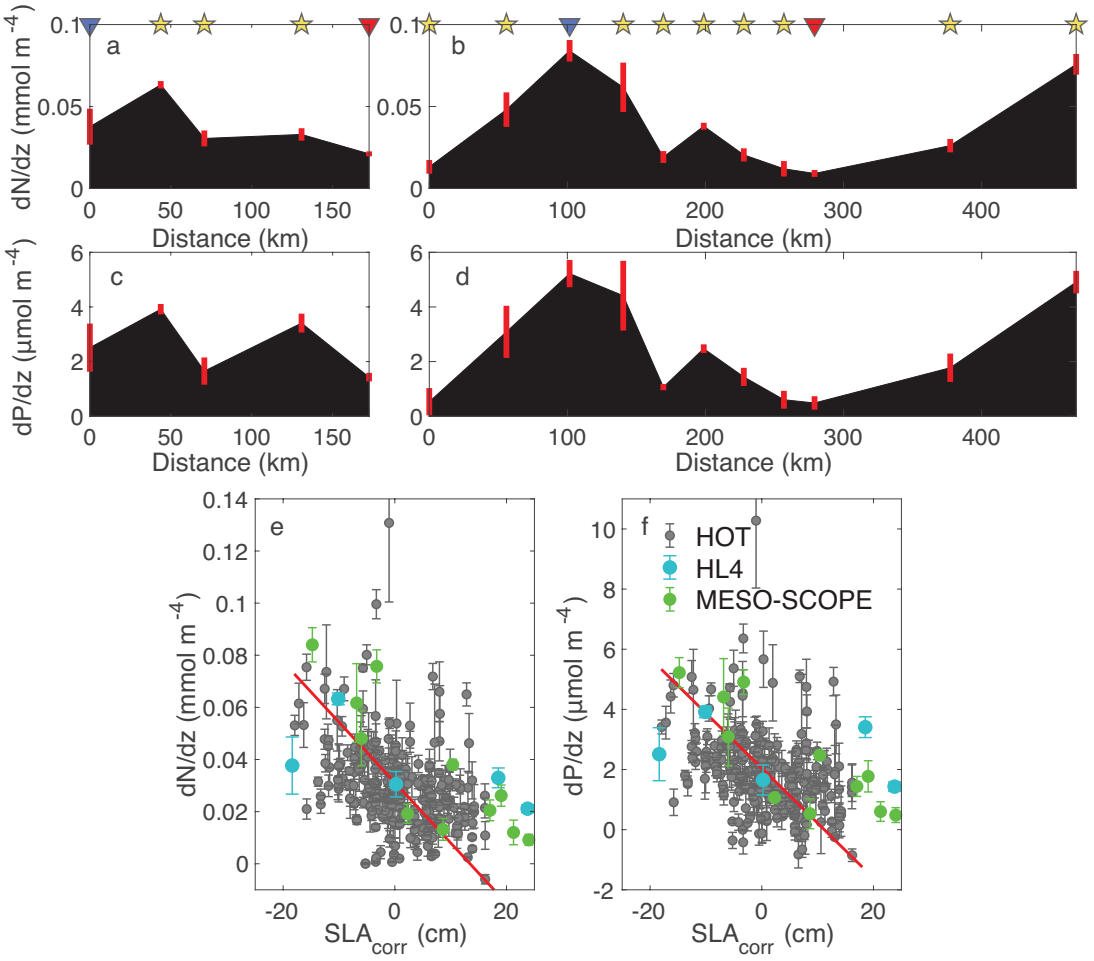

Figure 6: Changes in the vertical gradients of N+N (a,b) and PO_4^{3-} (c,d), defined as dN/dt and dP/dz, respectively, across adjacent eddies of opposite polarity for HL4 (a,c) and MESO-SCOPE (b,d) cruises. Panels e-f depict vertical gradients in N+N and PO_4^{3-} concentrations, respectively, versus SLA_{corr} for the two eddy transects (blue and green symbols) and the HOT program observations (gray symbols). Red lines in a-d and error bars in e-f depict ±1 standard deviation in the slopes. Red lines in e-f are linear regressions on HOT program nutrient gradients (Model II) with slopes of -0.0023 ± 0.0002 mmol m^{-4} cm^{-1} (r=0.36, $p=5\cdot10^{-9}$) and -0.00018 ± 0.00001 mmol m^{-4} cm^{-1} (r=0.35, $p=1\cdot10^{-8}$) for N+N and PO_4^{3-}, respectively. Estimates of vertical nutrient gradients were obtained by calculating the slope of the Model I linear regression of nutrient concentration versus depth in the vertical layer between 10 m above and 90 below the depth of the DCM.

We also examined relationships between the vertical nutrient gradients and SLA_{corr} based on the historical HOT program observations (Fig 6e,f). These analyses revealed patterns consistent with the more limited observations during HL4 and MESO-SCOPE. Specifically,

vertical gradients in concentrations of N+N and PO_4^{3-} decreased with increases in SLA_{corr} (Fig 6e,f).

3.4 Mesoscale variability in plankton biomass and community composition

Several consistent patterns in the near-surface waters and at the DCM emerged based on various proxy measurements of plankton biomass at the centers of both pairs of cyclones and anticyclones. In the near-surface waters, there were no apparent eddy-specific differences in concentrations of PC or beam attenuation, nor in chlorophyll *a* concentrations or fluorescence (Figure 7). In contrast, at the depth of the DCM, all of these proxy measurements of plankton biomass were elevated in the cyclonic eddies relative to the anticyclones. The concentration of PC was greater in the DCM of the cyclones relative to anticyclones by 1.3- and 1.4-fold, in the two expeditions (Figure 7a). Similarly, the concentration of chlorophyll *a* was greater in the DCM of the cyclones relative to anticyclones by1.2- and 1.3-fold (Figure 7c). This difference was even more pronounced for in situ chlorophyll fluorescence (Figure 7d), which includes contributions from pigments other than chlorophyll *a* and can be influenced by variation in fluorescence yield (Roesler et al., 2017). Fluorescence in the DCM was 1.3- and 1.8-fold greater in the cyclonic eddies than in the anticyclones (Figure 7d). Similarly, beam attenuation, an optical proxy for particle concentrations, was 1.4- and 1.5-fold greater at the depth of DCM in the cyclonic eddies relative to the anticyclones (Figure 7b) suggesting enhancement of plankton biomass rather than photoacclimation as drivers of these signals.

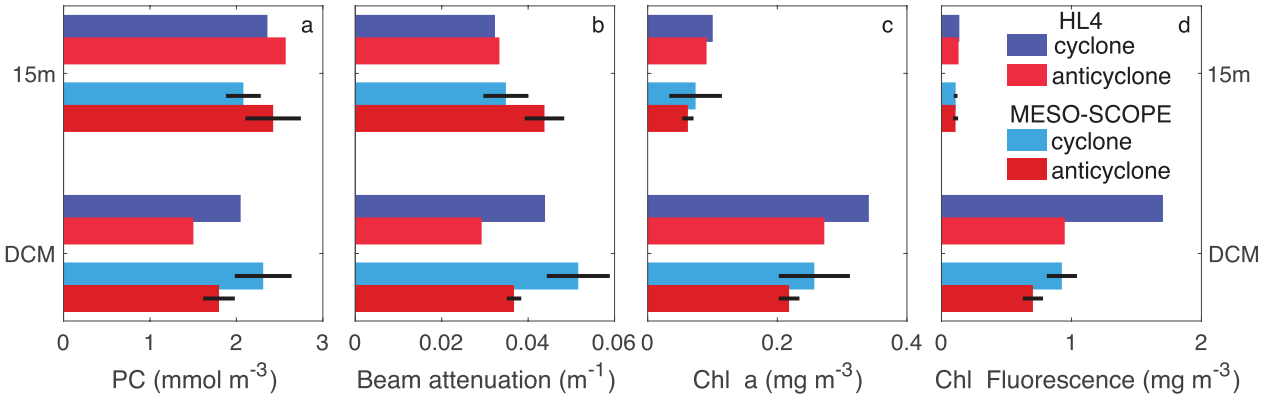

Figure 7: Average particle and pigment concentrations at 15 m and at the depth of the DCM in the centers of the cyclones (blue) and anticyclones (red) sampled as part of this study. Panels a) and b) depict the concentrations of PC and in situ optical measurements of beam attenuation, respectively. Panels c) and d) depict the concentration of chlorophyll *a* (Chl. a) and in situ optical measurements of chlorophyll fluorescence, respectively. Data points in panels b) and d) were isolated from the same deployments and depths used in samples a) and c). Black lines depict ±1 standard deviation of the mean, and are absent when only 1 measurement was available. The top 4 bars depict observations from 15 m, while the bottom 4 bars depict observations from the DCM. For the HOE-Legacy 4 cruise, the concentrations of PC and chlorophyll *a* at 15 m were obtained by averaging measurements collected at 5 and 25 m. For the MESO-SCOPE cruise, measurements associated with the Lagrangian sampling periods were used.

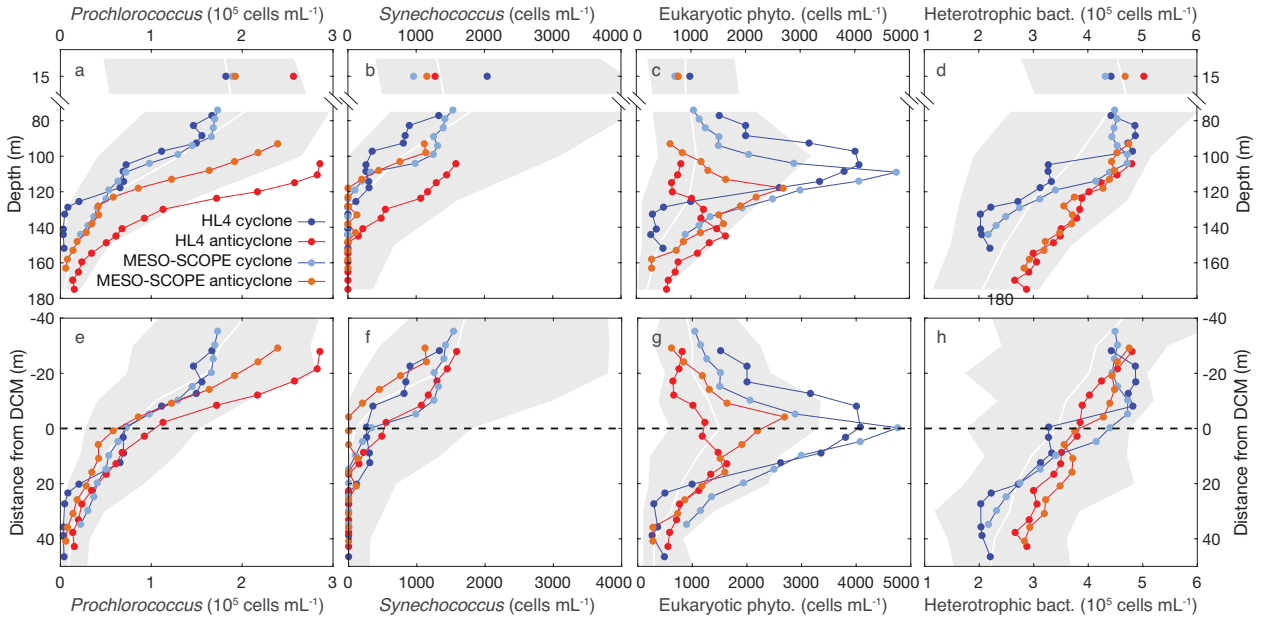

Figure 8: Average abundances of *Prochlorococcus*, *Synechococcus,* eukaryotic phytoplankton, and heterotrophic bacteria in the centers of the adjacent eddies derived from flow cytometry. Panels a-d) depict vertical profiles of cell abundances at depths bracketing the DCM in each eddy; the mean cell abundances measured at 15 m are also shown. Panels e-h) depict the same profiles shown in panels a-d), but the vertical axes are scaled relative to the depth of the DCM (positive values are deeper). White lines depict the median and shaded areas are the 5th and 95th percentiles of

HOT program measurements of these abundances. For the HOE-Legacy 4 cruise, abundances at 15 m were calculated as the average of measurements at 5 and 25 m. For the MESO-SCOPE cruise, abundances are averaged from sample collections during the Lagrangian sampling periods.

We also evaluated the abundances of *Prochlorococcus, Synechococcus*, eukaryotic phytoplankton, and heterotrophic bacteria in the adjacent eddy pairs based on flow cytometric analyses. We found that *Prochlorococcus* abundances were greater in the waters above the DCM in both anticyclones, relative to the cyclones, and relative to the HOT program climatology (Figure 8a,e). In contrast, eukaryotic phytoplankton (restricted to pico- and nanoplankton) abundance was elevated in a broad layer near the DCM. Maximum abundance in this layer exceeded the 95th percentile of HOT observations, with abundances in these eddies >4000 cells mL^{-1} (Figure 8c,g). Eukaryotic phytoplankton abundances in the near-surface waters were similar among the sampled eddies. Vertical distributions of *Synechococcus* were similar among the sampled eddies and similar to the HOT program observations of this genus (Figure 8b,f). Heterotrophic bacteria were more abundant in anticyclones than in cyclones in the near-surface and in waters below the DCM, but this pattern was reversed at depths just above the DCM.

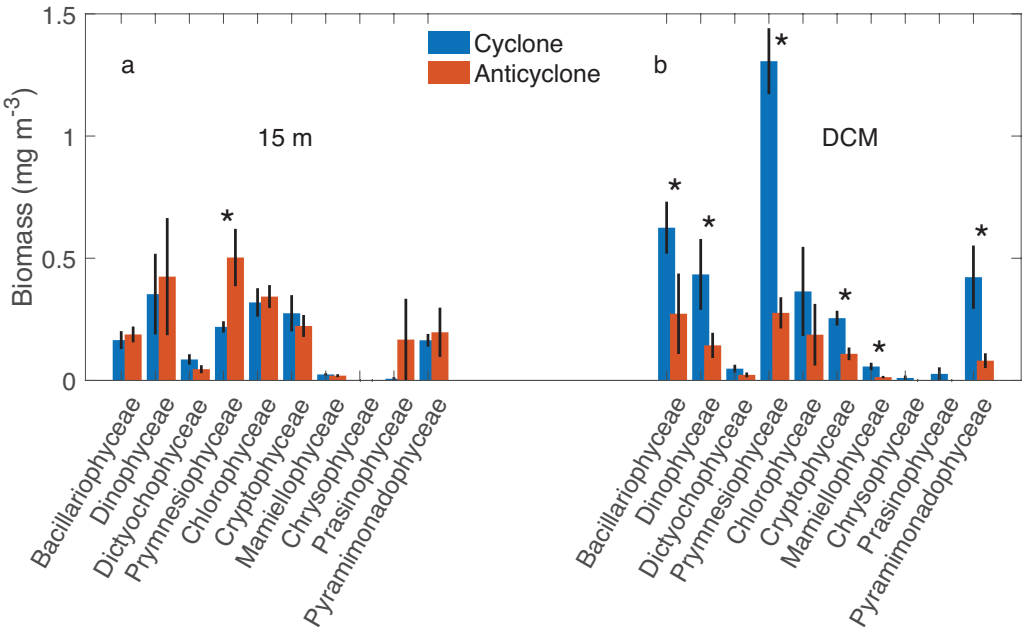

Figure 9: Mean biomass of nano- and microplanktonic (4-100 μm diameter) phytoplankton cells in the (a) near-surface ocean and (b) at the depth of the DCM at the cyclone (blue bars) and anticyclone (red bars) centers sampled during the MESO-SCOPE cruise. Bars depict mean of 7-8 discrete samples collected over 1 day and error bars are ± 1 standard error of the mean. Asterisks depict significant differences in biomass between cyclones and anticyclones (Wilcoxon rank sum test $p<0.05$).

During the MESO-SCOPE cruise, we also examined eddy-driven variability in the biomass of larger eukaryotic phytoplankton cells (4-100 μm in equivalent spherical diameter) imaged with an IFCb. In the near-surface waters, biomass estimates of most of the enumerated phytoplankton were similar between the eddies, with the exception of significantly greater biomass of Prymnesiophyceae in the anticyclone (Figure 8, Wilcoxon rank sum test $p<0.05$). Conversely, at the depth of the DCM, most phytoplankton classes demonstrated greater biomass in the cyclone than in the anticyclone (Figure 9). The dominant classes in the DCM of the cyclone were Prymnesiophyceae and Bacillariophyceae (specifically members of diatoms), whose biomass was 2.3 and 4.7 times greater than in the anticyclone, respectively (Figure 9b). Prymnesiophyceae genera, whose biomass was significantly larger in the DCM of the cyclone compared to the anticyclone (Wilcoxon rank sum test $p<005$), included *Phaeocystis*, *Ophiaster*, *Umbellosphaera*, *Acanthoica*, *Gephyrocapsa*, and *Syracosphaera* (in descending order of average biomass). The Bacillaryophceae genera enriched in the DCM of the cyclone were *Pseudo-nitzschia*, *Chaetoceros*, *Cylindrotheca*, and *Navicula*. Members of the Prymnesiophyceae and Bacillariophyceae are important controls on the formation of calcium carbonate and opal, respectively.

3.5 Mesoscale variability in particle export

Drift tracks of the sediment trap arrays were consistent with geostrophic circulation of the two eddies sampled during MESO-SCOPE (Figure 10a,b). The resulting particle fluxes measured across the adjacent eddies revealed clear mesoscale structure in both the magnitude and

559 stoichiometry of exported particulate matter export. Most notably, despite similarities in POC,
560 PN, and PPO_4^{3-} fluxes across the eddies, total mass, PSi, and PIC export were approximately 2-,
561 4-, and 2.9-fold greater, respectively, in the cyclone relative to the anticyclone (Figure 10c,d;
562 Supplementary Table S1). Moreover, total mass, PSi, and PIC fluxes were all inversely related to
563 SLA_{corr} (Figure 10c,d; Supplementary Table S1). In contrast, fluxes of POC, PN, and PPO_4^{3-} did
564 not vary significantly with spatial variations in SLA_{corr} (Figure 10; Supplementary Table S1;
565 Model II least-squares linear regressions, $p > 0.05$). In the cyclone, export of PIC accounted for
566 17% of the PC flux, with PIC comprising a lower fraction (~10%) of PC flux in the anticyclone
567 (Table 1). The proportions of PIC and PSi to mass flux were inversely related to spatial changes
568 in SLA_{corr}, with PIC:mass flux ratios (g $CaCO_3$:g total mass) decreasing from 38% to 28%, and
569 PSi:mass flux ratios (g Si:g total mass) varying from 2.5% to 1.4% across the cyclone to
570 anticyclone transect (Table 1). Because of the proportionally greater contribution of PIC and PSi
571 to mass flux in the cyclonic eddy, POC to mass flux (g C:g total mass) was positively related to
572 SLA_{corr}, with POC representing upwards of 34% of mass flux in the anticyclone and only ~22%
573 in the cyclone (Table 1). In addition to evaluating mesoscale spatial variation in fluxes of key
574 bioelements, we also quantified changes in δ^{15}N-PN. The δ^{15}N-PN of exported particles was
575 inversely related to changes in SLA_{corr} across the dipole, with the cyclone exporting PN with a
576 δ^{15}N signature as great as ~4.3‰, decreasing to as low as 3.0‰ in the anticyclone (Table 1).
577 The elevated contributions of PSi and PIC to particle export in the cyclonic eddy resulted in
578 significant spatial differences in the elemental stoichiometry of particulate matter export across
579 the mesoscale field. Elevated PSi flux in the cyclone coincided with decreasing POC:PSi,
580 PN:PSi, and PPO_4^{3-}:PSi ratios (mol:mol) across the eddies (Table 1). Moreover, all three ratios
581 were positively correlated to changes in SLA_{corr}. Elevated fluxes of PIC within the cyclonic eddy

582 resulted in decreasing PC:PIC, PN:PIC, and PPO_4^{3-}:PIC ratios across the cyclone to anticyclone
583 transect, with all three ratios inversely related to spatial changes in SLA_{corr} (Table 1). In contrast,
584 POC: PPO_4^{3-} and PN: PPO_4^{3-} ratios (mol:mol) did not vary with SLA_{corr}, averaging 173 (±20) and
585 28 (±2.0), respectively. Intriguingly, although neither POC nor PN fluxes varied significantly
586 with SLA_{corr}, the ratio of POC:PN was inversely and significantly related to SLA_{corr} (Table 1).
587 Once again, we leveraged HOT program observations to evaluate the generality of the
588 mesoscale variability of particle fluxes across eddies. In this instance, we assessed the
589 significance and strength of the Pearson correlations between HOT particle fluxes and SLA_{corr}.
590 Consistent with our sampling during MESO-SCOPE, we find a lack of correlation between
591 SLA_{corr} and sinking fluxes of PC, PN, and PPO_4^{3-}, but significant negative correlations in fluxes
592 of both PSi and PIC and SLA_{corr} (Supplementary Table S1; $p < 0.05$). While the negative
593 correlations of PSi and PIC are consistent with observations during MESO-SCOPE, we also
594 found a significant positive correlation for HOT observations between $\delta^{15}N$ and SLA_{corr}
595 (correlation coefficient of 0.14; $p < 0.05$), which was opposite in sign of the relationship observed
596 based on the MESO-SCOPE sediment trap collections.

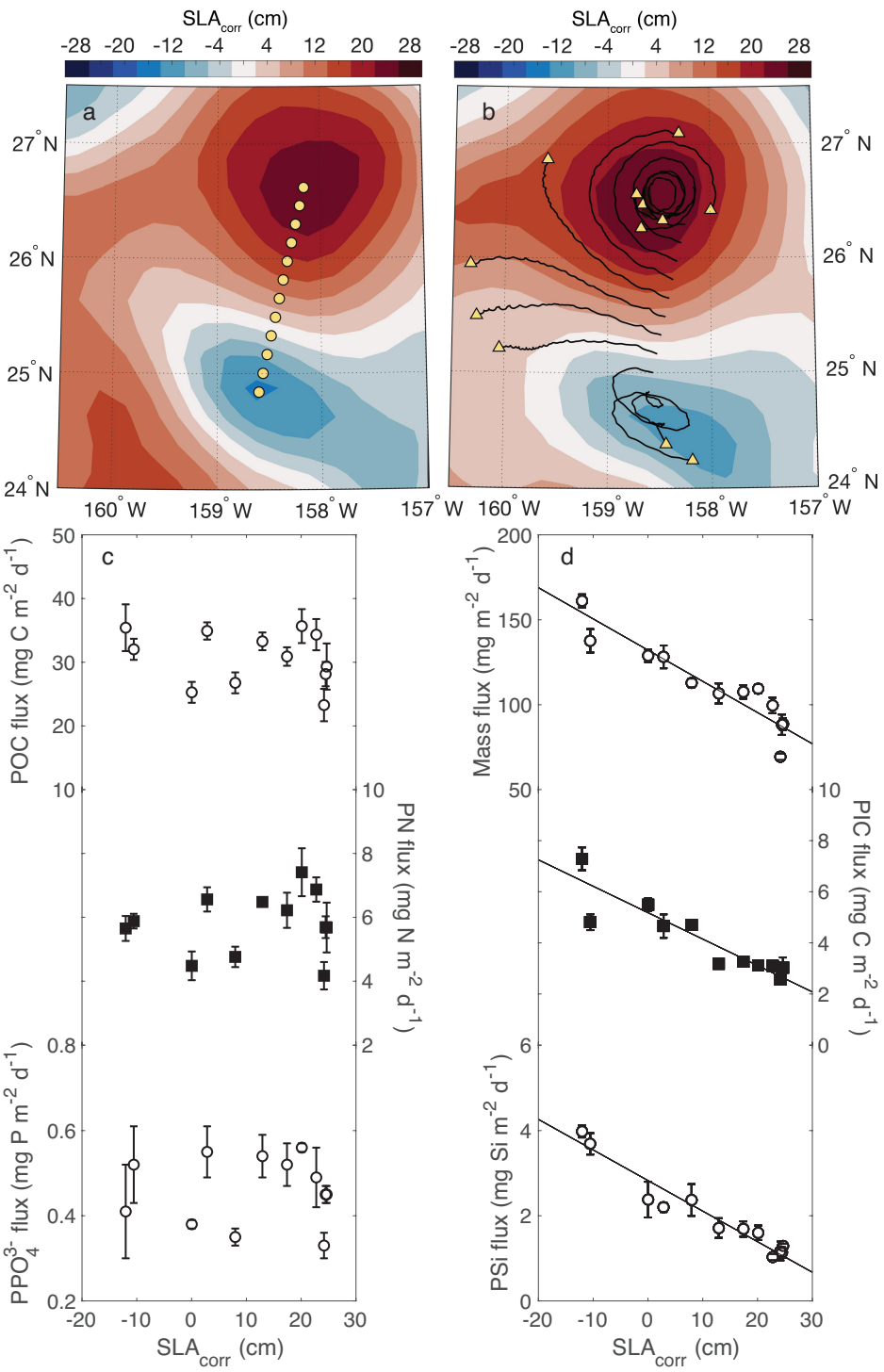

Figure 10: Results from sediment trap array deployments during the MESO-SCOPE eddy survey. a) Coordinates of the 12 individual, free-drifting particle interceptor trap arrays at the time of deployment superimposed on the map of SLA_{corr} for July 2; b) Spatial drift tracks of the particle interceptor traps deployed during the MESO-SCOPE expedition superimposed on the map of SLA_{corr} on July 14; c) Variability of the fluxes of POC, PN, and PPO_4^{3-} with SLA_{corr}; d) Relationships between fluxes of total mass, PIC, and PSi with SLA_{corr}. Lines in d) depict the Model II linear regressions.

604 *3.6 Numerical simulation of the mesoscale variability at Station ALOHA*

605 We used the results of a four-dimensional numerical simulation at Station ALOHA to
606 investigate if the mesoscale variability observed in the field expeditions and HOT program
607 sampling could be reproduced by ecological dynamics captured with the model. Doing so
608 revealed several intriguing similarities and differences between the model results and the
609 empirical observations. The difference between the median potential density measured during
610 HOT and simulated by the model never exceeded 0.1 kg m^{-3} in the upper 175 meters
611 (Supplementary Figure 1). The simulation and field results converged on vertical association of
612 the DCM and the depth of the nutricline (Supplementary Figure 1). However, the model results
613 underestimated concentrations of chlorophyll *a* and primary production in the upper 100 m, and
614 overestimated nutrient concentrations below 75 m (Supplementary Figure 1). Notably, regression
615 analyses of the depth of the 24.6 kg m^{-3} isopycnal versus SLA_{corr} in the model results revealed a
616 vertical displacement of 3.2±0.0 m cm^{-1}, a mean value very similar to the field observations
617 derived from the HOT program (Barone et al., 2019).

618 We used the numerical model results to identify three patterns of mesoscale variability that
619 we highlighted from our field observations: 1) changes in the isopycnal nutrient concentration
620 with SLA_{corr} near the depth of the DCM; 2) changes in the steepness of the nutricline with
621 SLA_{corr}; and 3) changes in the biomass of eukaryotic phytoplankton at the DCM with SLA_{corr}.
622 Results from the simulation were consistent with our observations of an increase in the isopycnal
623 nutrient anomaly with SLA_{corr} (Figure 11a) and of decreases in the vertical nutrient gradients and
624 eukaryotic phytoplankton biomass at the DCM with SLA_{corr} (Figure 11b,c). The change in
625 isopycnal nutrient concentration with SLA_{corr} was 0.059±0.001 mmol m^{-3} cm^{-1}, lower than the
626 value of 0.102±0.008 observed in the HOT program observations. Similarly, the change in the

steepness of the nutricline in the model (-0.0016±0.0000 mmol m^{-3} cm^{-1}) was lower than the change observed during HOT (-0.0023±0.0002 mmol m^{-3} cm^{-1}). The HOT program does not specifically measure eukaryotic phytoplankton biomass among different size plankton classes; hence, we could not directly compare the model simulation to those of the field observations.

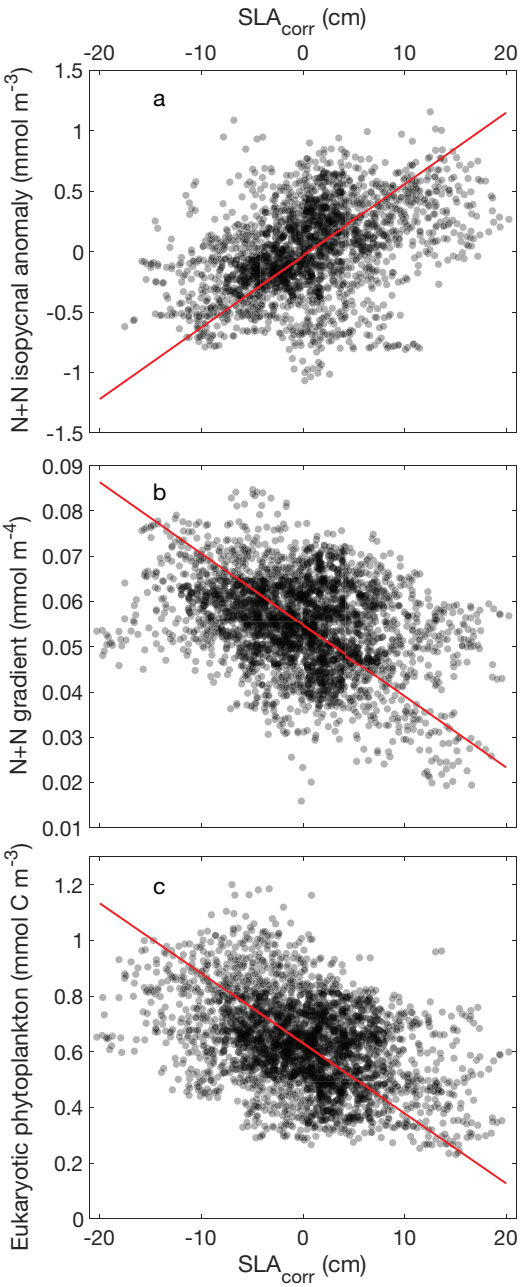

Figure 11: Results from a general circulation model (MITgcm) including a multi-species ecological component (Darwin) extracted at Station ALOHA between 1993 and 2015. Co-variation of SLA_{corr} with: a) monthly anomaly of

the concentration of N+N on the 24.5 kg m^{-3} isopycnal after removing the long-term trend (365 days running mean) (slope = 0.059±0.001 mmol m^{-3} cm^{-1}, r=0.41, p=3.4·10^{-86}); b) vertical gradients of N+N concentration near the depth of the DCM (slope = -0.00157±0.00003 mmol m^{-4} cm^{-1}, r=0.35, p=2.1·10^{-80}); c) eukaryotic phytoplankton biomass at the depth of the DCM (slope = -0.0251±0.0005 mmol C m^{-3} cm^{-1}, r=0.41, p=5.1·10^{-111}). Solid lines depict the Model II linear regressions.

4. Discussion

4.1 Mesoscale impacts on the nutricline and on the lower euphotic zone

On two separate research cruises in the subtropical North Pacific Ocean, we sampled pairs of adjacent mesoscale eddies of opposite polarity in late spring and summer, providing an opportunity for comparative analyses of upper ocean biogeochemistry and plankton ecology associated with mesoscale features in close (<200 km) spatial proximity. Based on these analyses, we identified common features associated with eddies of similar polarity and we then used the time-resolved, Eulerian HOT program observations to evaluate the generality of mesoscale disturbances on the behavior of the upper ocean in this oligotrophic habitat. Notably, our findings suggest that mesoscale motions have a large impact on plankton biogeochemistry in the lower euphotic zone, but such dynamics are not as apparent in the well-lit near-surface ocean. These results are consistent with a previous study that found time-varying mesoscale dynamics structured much of the temporal variability in temperature and nutrient stoichiometry in the dimly-lit lower euphotic zone at Station ALOHA, but had limited influence on these properties through the well-lit upper ocean (Church et al. 2009). In the current study, by coupling our sampling of adjacent eddies with a multi-decadal analysis of HOT program observations, we find robust differences between cyclones and anticyclones in concentrations of chlorophyll *a*, dissolved O_2, inorganic nutrients, and particle load in the lower euphotic zone. However, differences in these properties were not apparent in the well-lit upper ocean waters.

The consistent biogeochemical responses to mesoscale motions observed in the lower euphotic zone reflect rapid plankton assimilation of nutrients with concomitant increases in eukaryotic phytoplankton biomass, as the nutricline undergoes mesoscale-driven oscillations across the exponentially varying light field. This variability in the lower euphotic zone is consistent with previous findings on the change in the vertical distributions of nutrients and biomass related to mesoscale activity at Station ALOHA (Church et al., 2009; Barone et al., 2019). The eddies sampled as part of this study bracketed the full dynamic range of SLA_{corr} variability observed at Station ALOHA and revealed that mesoscale motions can vertically perturb isopycnals in the lower euphotic zone by more than 100 m. The large vertical excursions of isopycnals near the DCM alter the ambient light field by more than an order of magnitude (*e.g.,* during MESO-SCOPE measured light fluxes along the 24.5 kg m^{-3} isopycnal varied 0.11 to 3.4 moles photon m^{-2} d^{-1} between the anticyclone and the cyclone). Such large variations in light intensity would be expected to stimulate phytoplankton production in the light-limited DCM (Goldman 1993; Goldman and McGillicuddy 2003; Li et al. 2011), with concomitant impacts on concentrations of nutrients and dissolved O_2, a finding consistent with our analyses of historical HOT program observations. The dynamics identified in this study may be a common feature of oligotrophic ocean ecosystems during those periods of the year when the base of the mixed layer remains vertically well separated from the top of the nutricline. This vertical separation, coupled with rapid assimilation of inorganic nutrients by the plankton community in the DCM layer, limits the impact of mesoscale eddies on phytoplankton growing in the well-lit, near-surface oceans.

It has been previously proposed that the mesoscale stimulation of phytoplankton activity is limited to the intensification stage of cyclonic eddies (Sweeney et al., 2003; Rii et al., 2008). Our

observations extend this model: we observed an increase in phytoplankton biomass in the DCM of cyclonic eddies several weeks after their intensification (eddy life cycles in Supplementary information). These observations suggest that mesoscale delivery of inorganic nutrients to the lower euphotic zone is not limited to the active upwelling phase of the eddy life cycle (the intensification stage), but continues well into the mature phase of an eddy. We propose continued nutrient delivery to the lower euphotic zone is maintained late into the lifetime of cyclonic eddies due to the steepening of the vertical nutrient gradients that accompanies vertical uplift of the thermocline and subsequent biological erosion of the top of the nutricline. In subtropical gyres, the DCM is often vertically associated with the top of the nitracline (Herbland and Voituriez, 1979; Cullen and Eppley, 1981; Bahamón et al., 2003; Letelier et al., 2004), here defined as the layer where inorganic nitrogen concentrations start increasing with depth, and where turbulent mixing provides an upward flux of inorganic nitrogen to the euphotic zone (Lewis et al., 1986; Anderson, 1969). The vertical positioning of both these features appears structured by light; during isopycnal uplift that accompanies cyclones, light-limited phytoplankton communities are vertically transplanted upward across the exponentially increasing light field, stimulating net productivity (as reflected in increased eukaryotic phytoplankton biomass), producing O_2 and consuming nutrients.

Based on analyses of the vertical concentration gradients in inorganic nutrients due to isopycnal heaving, we estimate the role of eddies in driving diapycnal fluxes of inorganic nutrients into the euphotic zone. This analysis assumes that changes in the first vertical derivative in nutrient concentrations are not counterbalanced by opposite changes in diapycnal eddy diffusivity. Under this assumption, we find that vertical displacement of the nutricline associated

703 with cyclones increases net diapycnal fluxes of N+N and PO_4^{3-} by upwards of 9-fold and 11-fold,
704 respectively, relative to anticyclones (Figure 6).

705 To explain our observations, we propose a conceptual framework that describes the temporal
706 dynamics associated with cyclonic uplift of the nutricline in the stratified ocean (Figure 12). Prior
707 to the intensification of the cyclonic eddy, the biomass maximum of eukaryotic phytoplankton
708 coincides with the DCM, at a depth determined by the downward light flux (Figure 12a; Letelier
709 et al., 2004). Mesoscale uplift results in upward displacement of the DCM community and the
710 nutricline, increasing light in layers where its flux otherwise limits phytoplankton growth (Figure
711 12b). As a response to this uplift, phytoplankton utilize the additional light energy available,
712 increasing in biomass and consuming the available nutrients. This upward isopycnal
713 displacement drives increases in net photosynthetic production, and over time results in a
714 "chemical wake," observed as a negative nutrient anomaly (Figure 12c) and a positive O_2
715 anomaly in the waters above the DCM. One important consequence of nutrient removal by this
716 mechanism is a steepening of the nutricline and presumed intensification of diapycnal nutrient
717 fluxes, maintaining elevated eukaryotic phytoplankton biomass within the DCM (Figure 12c),
718 which now lies within denser waters.

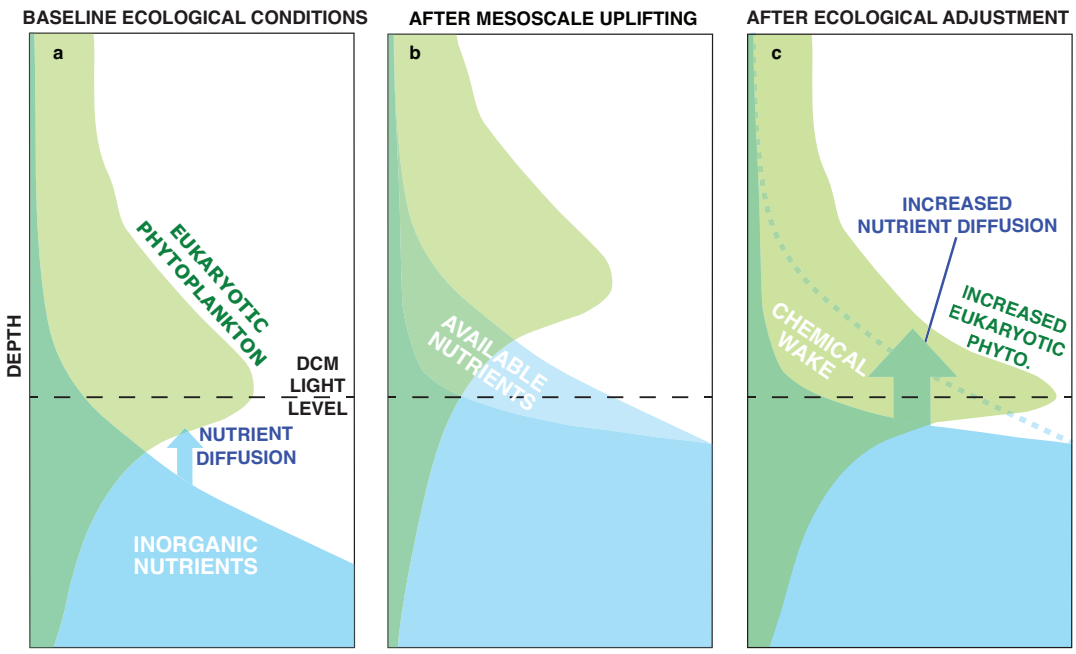

Figure 12: Ecological plankton dynamics in a mesoscale cyclone during three idealized steps: a) before the cyclone origin; b) after an instantaneous uplifting caused by eddy intensification; and c) after the ecosystem responds to the uplifting and a new DCM community emerges and consumes the inorganic nutrients made available by the uplifting of the nutricline.

The simplified conceptual framework depicted in Figure 12 synthesizes our view of biogeochemical dynamics associated with the uplift of the thermocline in cyclones, where increased nutrient delivery to the lower euphotic zone continues after the eddy intensification phase, a finding we attribute to increased vertical nutrient gradients. A link between SLA_{corr} and diapycnal nutrient fluxes had been previously noticed by Barone et al. (2019), but this study provides additional support that mature phase cyclonic eddies can continue to support phytoplankton production. We propose that net phytoplankton growth during eddy intensification erodes the top of the nutricline, evident in our study as a negative isopycnal anomaly of nutrient concentrations, which in turn increases diapycnal fluxes of nutrients into the lower euphotic zone during the mature phases of cyclonic eddies. We also utilized a four-dimensional numerical

735 model to investigate if the variability observed in our empirical observations were captured by a
736 dynamic ecosystem model, where light and nutrient limitation regulate phytoplankton growth
737 (Dutkiewicz et al., 2015). Analyses of the model results from Station ALOHA further supports
738 our conceptual framework linking erosion of the nutricline to diapycnal nutrient fluxes and
739 increased biomass of eukaryotic phytoplankton near the DCM during periods of low SLA_{corr}.
740 These results reinforce our conclusion that mesoscale oscillations of the thermocline coupled
741 with simple ecological dynamics lead to a modification of the characteristics of the lower
742 euphotic zone that extends the ecological impact of cyclonic eddies beyond their intensification
743 phase.
744
745 *4.2 Mesoscale alterations in O_2 and nutrient stoichiometry*
746 Our analyses on the biogeochemical variability along isopycnal surfaces showed that mesoscale
747 dynamics vertically decouple O_2 production from nutrient consumption. As an example, during
748 the MESO-SCOPE cruise, the 24.5 kg m^{-3} isopycnal was displaced upwards to a depth of 64 m in
749 the center of the cyclonic eddy, which was 65 m shallower relative to the position of the same
750 isopycnal in the anticyclone. This displacement increased the daily light flux to this isopycnal in
751 the cyclone by more than an order of magnitude relative to the mean light flux measured in the
752 center of the anticyclone (3.4 mol photons m^{-2} d^{-1} versus 0.11 mol photons m^{-2} d^{-1}). The increased
753 light presumably stimulated net community production, which was linked with an excess 23
754 mmol O_2 m^{-3} measured on the 24.5 kg m^{-3} isopycnal in the center of the cyclone with respect to
755 the average concentration measured during the eddy survey on the same isopycnal. Similarly,
756 inorganic nutrient consumption resulted in isopycnal concentration anomalies of N+N and PO_4^{3-}
757 of -0.21 mmol N m^{-3} and -0.043 mmol P m^{-3}, respectively. The resulting O_2:N and O_2:P molar

758 stoichiometries (110:1 and 535:1, respectively) suggested excess net O_2 production with respect
759 to the consumption of inorganic nutrients. This phenomenon was widespread in both cyclone
760 centers, where it was observed in a depth layer above the DCM approximately between 50 and
761 100 m, with an excess of O_2 with respect to N+N reaching values above 10 mmol m^{-3} (Figure 5).
762 Conversely, below 100 m, all eddy centers were characterized by a deficit in O_2 with respect to
763 the concentration expected based on inorganic nutrient concentrations (Figure 5). The
764 observation of similar variability in eddies of opposite polarity is intriguing considering the
765 isopycnal anomalies must sum to zero across each eddy transect, but it is possible that different
766 mechanisms produced the O_2 deficits in cyclones and anticyclones.
767 A number of previous studies, including several based at Station ALOHA, have reported
768 anomalous O_2 to nutrient stoichiometries similar to those described in this study. Using apparent
769 oxygen utilization (AOU; defined as $O_{2\ \text{solubility}} - O_{2\ \text{measured}}$) as a measure of the cumulative
770 respiratory consumption of O_2 that has occurred since a water parcel last ventilated with the
771 atmosphere, and assuming fixed stoichiometry between respiratory O_2 consumption and N
772 regenerated through mineralization, Emerson and Hayward (1995) found that O_2:N
773 stoichiometries deviated substantially from those expected based on Redfield mineralization of
774 organic matter in the lower euphotic zone and upper mesopelagic waters. More recently,
775 leveraging autonomous profiling floats equipped with O_2 and NO_3^- sensors, Johnson et al. (2010)
776 documented consistent supersaturation of O_2 in the well-lit euphotic zone waters and an apparent
777 deficit of NO_3^- (relative to respiratory O_2 consumption) at depth. Moreover, these authors found
778 that the "overproduction" of O_2 relative to NO_3^- consumed in the upper euphotic zone could be
779 balanced by the NO_3^- consumption without corresponding O_2 production at depth (Johnson et al.
780 2010). In a subsequent analysis of profiling float O_2 and NO_3^- data from the subtropical North

781 Pacific, Ascani et al. (2013) identified discrete stoichiometric “regimes”, differentiated by the
782 vertical position of the isopycnal surface. Similar to the current study, along isopycnal surfaces
783 typically confined to the upper euphotic zone, where nutrient concentrations were minimal, O_2
784 concentrations increased independent of measurable changes in NO_3^- (Ascani et al., 2013). In
785 contrast, O_2 and NO_3^- generally co-varied in near-Redfield proportions along isopycnals located
786 in the dimly-lit or dark waters of the upper ocean (Ascani et al., 2013).
787 Several mechanisms have been proposed as underlying the formation of anomalous ratios
788 in the concentration of O_2 and inorganic nutrients. Emerson and Hayward (1995) argue that
789 mineralization of dissolved organic matter that is substantially enriched in C relative to N and P
790 likely underlies the formation of anomalous O_2:N stoichiometries. A subsequent study by Abell
791 et al. (2005) used an along-isopycnal mass balance model to quantify mineralization of DOM as a
792 mechanism maintaining the anomalous stoichiometry observed in the lower euphotic zone,
793 concluding that mineralization of C-enriched DOM (i.e., C:N molar ratio of 30-32) could explain
794 the anomalous O_2 and nutrient stoichiometry. Similarly, Fawcett et al. (2018) argued that
795 production of C-rich organic matter in the well-lit euphotic zone, and subsequent consumption of
796 that material at depth, together with heterotrophic bacterial assimilation of NO_3^-, resulted in the
797 anomalous O_2 to nutrient stoichiometry observed in the Sargasso Sea. More recently, using
798 measurements from Station ALOHA, Letscher and Villareal (2018) argued additional processes,
799 namely phytoplankton vertical migration, must also be invoked to explain the apparent O_2 to
800 nutrient imbalance. Formation of nitrous oxide during nitrogen oxidation (e.g., ammonia or NO_2^-
801 oxidation) that occurs in the lower euphotic zone and upper mesopelagic waters would further
802 alter the stoichiometry of O_2 consumed relative to NO_3^- produced (Wilson et al. 2014). Based on
803 our eddy-centric observations, it appears different mechanisms may be best suited to explain the

anomalies in anticyclones and in cyclones. In anticyclones, the subduction of near-surface water could provide high concentrations of C-rich organic matter to the lower euphotic zone, which would be later mineralized and result in lower O_2 concentrations relative to concentrations of inorganic nutrients that would be produced if the organic matter were mineralized in typical (i.e., Redfieldian) stoichiometry. Conversely, vertically-migrating phytoplankton might consume nutrients near the top of the nutricline and actively move upward to photosynthesize (Villareal et al. 1993), which could explain both the O_2 deficit below 100 m (where nutrients are taken up without O_2 production) and the O_2 surplus in the 50-100 m layer (where O_2 is produced without nutrient uptake) in the cyclonic eddies.

4.3 Mesoscale variability in particle fluxes

By deploying a suite of 12 individual, drifting sediment trap arrays across two adjacent eddies of opposite polarities we obtained spatially-resolved information on particle export across a large mesoscale gradient (SLA_{corr} for these deployments ranged between -12 cm to 25 cm). Although export of organic matter (POC, PN, and PPO_4) was similar across and within this mesoscale gradient, total mass flux varied more than 2-fold, coincident with approximately 4-fold changes in export of PSi and PIC. Export of total mass, PSi, and PIC were all greatest in the cyclone center (lowest SLA_{corr}) and decreased linearly with increases in SLA_{corr}. Moreover, the $\delta^{15}N$ signature of sinking PN points to differing sources of N supporting export across these eddies. While these observations were collected in strong mesoscale eddies, they depict several patterns of particle flux variability broadly linked with different classes of mesoscale motions, as demonstrated by the analysis of historical observations from the HOT program. Consistent with measurements in MESO-SCOPE, the HOT particle fluxes of PC, PN, and PPO_4 were not

827 significantly correlated with SLA_{corr}, a finding previously reported by Barone et al. (2019), while
828 a negative correlation was observed for PIC and PSi. Conversely, the increased $\delta^{15}PN$ in the
829 MESO-SCOPE cyclone is in the opposite direction of the HOT positive correlation of $\delta^{15}PN$ and
830 SLA_{corr}.

831 To put our observations into context, it has been previously proposed that the upwelling of
832 nutrient-rich water during the intensification of cyclonic eddies is a major cause of mesoscale
833 variability in particle fluxes (Sweeney et al., 2003; Rii et al., 2008). However, we believe that our
834 observations are not directly linked to this process, for two main reasons: 1) the correlations of
835 particle fluxes with SLA_{corr} point to a connection with the depth of the thermocline rather than
836 with the vertical velocities that would be associated with eddy intensification or weakening; and
837 2) the cyclone sampled during MESO-SCOPE had its nearest intensification event 32 days before
838 our sampling (Supplementary information). As a consequence, we postulate that the mesoscale
839 variation detected in our measurements is a product of the shallower and steeper nutricline at low
840 SLA_{corr}, which sustains a more abundant population of eukaryotic phytoplankton, including
841 diatoms and prymnesiophytes, with subsequent impact on the export of biomineralized particles.
842 In contrast, the deeper nutricline in anticyclonic eddies appears to favor the proliferation of small
843 picoplanktonic cyanobacteria (i.e., *Prochlorococcus*; Barone et al. 2019). The MESO-SCOPE
844 anticyclonic eddy also contained nearly twice the concentration of dissolved iron than is typically
845 found at the DCM at Station ALOHA, which may have supported the increase in
846 *Prochlorococcus* abundance near the DCM (Hawco et al., companion submission).

847 One of the most striking observations from the MESO-SCOPE sediment trap deployments
848 were the robust inverse relationships between SLA_{corr} and PSi, PIC, and total mass flux.
849 Enhanced PSi export has been previously reported for a wind-driven cyclone south of the

850 Hawaiian archipelago (Benitez-Nelson et al., 2007; Rii et al., 2008); however, our observations
851 provide evidence that cyclonic eddies may also promote PIC export. To our knowledge, these are
852 the first observations linking export of PIC to mesoscale dynamics. The enhanced fluxes of PSi
853 and PIC observed during MESO-SCOPE provides some insights into the phytoplankton likely
854 fueling particle export in the cyclone, specifically diatoms and prymnesiophytes, whose biomass
855 was elevated in the DCM of the cyclone relative to the DCM of the anticyclone. Diatoms and
856 prymnesiophytes are key phytoplankton taxa containing opal and calcium carbonate, but some
857 large zooplankton of the group Rhizaria also have mineral skeletons of calcium carbonate (e.g.,
858 Foraminifera) or opal (e.g., Radiolaria). We could not quantify the abundance of large Rhizaria
859 (>100μm in diameter) with the methods employed in this study so we cannot exclude
860 contributions from these organisms to the observed variations in the export of PSi and PIC
861 between eddies of different polarity. A number of previous studies have identified elevated
862 diatom and prynmnesiophyte biomass in the DCM of cyclonic eddies (Bidigare et al., 2003;
863 Benitez-Nelson et al. 2007; Rii et al., 2008). In a microscopy-based assessment of diatoms,
864 Scharek et al. (1999) found low contributions to sinking particle export by members of the DCM
865 diatom assemblage, but they noted how a substantial fraction of the diatom frustules were empty
866 (lacking cytoplasm). Similarly, Benitez-Nelson et al. (2009) concluded that coupling between
867 phytoplankton growth and microzooplankton grazing in Hawaiian lee cyclones resulted in export
868 of empty diatom frustules, thereby increasing the PSi:POC ratio of the trap-derived material.
869 Based on pigment and gene-based analyses, Li et al. (2013) concluded that diatoms and
870 prymnesiophytes comprised approximately 2% and 20%, respectively, of total chlorophyll *a* in
871 the lower euphotic zone at Station ALOHA. However, the proportion of diatom and
872 prymnesiophyte genes exported, relative to the euphotic zone inventory, averaged 0.15% d^{-1} and

873 0.19% d^{-1}, compared to the 5% d^{-1} PSi export : inventory (Li et al., 2013). These results appear
874 consistent with the interpretation that empty diatom frustules and calcified liths underlie the
875 elevated PSi and PIC fluxes in the MESO-SCOPE cyclone.
876 In addition to clear relationships between mass, PSi, and PIC fluxes, the $\delta^{15}N$ of the exported
877 PN demonstrated a significant inverse relationship to SLA_{corr} during MESO-SCOPE (i.e., the
878 $\delta^{15}N$ of PN was more enriched in the cyclone relative to the anticyclone). A number of previous
879 studies have utilized a two-end member isotope model, leveraging differences in the $\delta^{15}N$
880 signatures of deep water NO_3^- and N_2, to estimate the proportion of PN export supported by NO_3^-
881 assimilation and N_2 fixation at Station ALOHA (Karl et al., 1997; Dore et al., 2002; Casciotti et
882 al., 2008; Böttjer et al. 2016). Assuming only two potential sources of N (NO_3^- assimilation and
883 N_2 fixation) support PN export, these observations suggest that NO_3^- assimilation was relatively
884 more important in the cyclone (where NO_3^- appeared to support upwards of 85% of PN export)
885 while N_2 fixation was relatively more important in the anticyclone (where N_2 fixation was
886 estimated to support upwards of 40% of PN export). While it would be tempting to attribute the
887 $\delta^{15}N$ variability to changes in the diapycnal fluxes of NO_3^- linked with changes in the steepness
888 of the nutricline, this is probably not the case: Based on the observations from the HOT program,
889 we found steepening of the nutricline with decreasing SLA_{corr}, but a positive correlation between
890 $\delta^{15}N$ and SLA_{corr}, opposite in sign to the variation observed during MESO-SCOPE. Since
891 diapycnal fluxes were likely not driving the change in $\delta^{15}N$ across eddies, this variation might
892 have been supported by high rates of N_2 fixation by the abundant diazotroph *Crocosphaera*
893 measured in the MESO-SCOPE anticyclone (Dugenne et al., 2020). A number of previous
894 studies have documented increases in N_2 fixation and N_2-fixing microorganism biomass
895 associated with anticyclonic eddies (Davis and McGullicuddy, 2006; Fong et al., 2008; Wilson et

al., 2017). During the warm summer months (June-October), rates of N_2 fixation at Station ALOHA often peak during periods of positive SLA_{corr} such as those associated with anticyclones (Church et al., 2009; Böttjer et al., 2016). The gradient in $\delta^{15}N$ of PN export across the mesoscale eddies sampled in the current study further reinforce the apparent promotion of N_2 fixation in anticyclones during the summer.

In the NPSG, the mesoscale delivery of inorganic nutrients to the euphotic zone through upwelling is larger than the delivery caused by changes in diapycnal mixing (Barone et al., 2019). While we think that upwelling was not responsible for the variability in particle fluxes across eddies observed in this study, its effect is clearly evident in the positive isopycnal anomalies of O_2 and negative isopycnal anomalies of inorganic nutrients measured in cyclones. So what was the fate of the POC, PN, and PPO_4 synthesized to produce the isopycnal O_2 anomalies before we sampled the eddies? During HL4 and MESO-SCOPE, 50-200 m depth integrated O_2 saturation anomalies (taking into account changes in solubility) in the cyclone centers were 2152 mmol O_2 m^{-2} and 772 mmol O_2 m^{-2}, respectively, suggesting excess O_2 produced in the lower euphotic zone was not accompanied by concomitant consumption of O_2 via respiration of organic matter in the top of the mesopelagic zone. Suspended PC inventories during HL4 and MESO-SCOPE appear too low to account for the formation of O_2 isopycnal anomalies. Furthermore, we did not measure dissolved organic carbon, but concentrations of dissolved organic N and P were lower in the cyclone than in the anticyclones (data not shown). Such findings suggest that the organic matter produced which resulted in the cyclone O_2 anomalies likely was no longer in the dissolved and particulate stocks in the upper ocean, but rather had already been exported to deeper waters, presumably through particle settling or through the action of vertically migrating zooplankton. As a consequence, the biogeochemical signatures associated with nutrient consumption and O_2

production remained in the euphotic zone as a “chemical wake”, reflecting the prior history of productivity and export associated with cyclonic uplift of the isopycnal surfaces. Taken together, the isopycnal anomalies and sediment trap fluxes indicate that the MESO-SCOPE cruise likely sampled the cyclonic eddy at some point after the peak period of organic matter export, and that the PSi and PIC export patterns reflected settling of empty diatom frustules and calcified liths from the DCM phytoplankton community, which was sustained by the enhanced diapycnal nutrient fluxes during the mature stage of the eddy.

5. Conclusions

By sampling adjacent eddies of opposite polarity we identified several impacts of mesoscale motions on plankton biology and upper ocean biogeochemistry in the subtropical North Pacific Ocean. Some key findings that emerged from our study are:

1. Cyclonic isopycnal uplift increased vertical gradients in inorganic nutrients through the biological erosion of the top of the nutricline. This presumably increased the diapycnal flux of nutrients delivered to the lower euphotic zone and supported increased eukaryotic phytoplankton biomass. Conversely, depression of isopycnals in anticyclones decreased nutrient concentration gradients in the lower euphotic zone, a dynamic that appeared to increase *Prochlorococcus* biomass above the DCM.
2. Mesoscale changes in inorganic nutrients and dissolved O_2 concentrations are vertically decoupled. For example, upward displacement of isopycnals associated with cyclonic eddies resulted in peak consumption of inorganic nutrients occurring deeper than the layer where O_2 production was maximal. In contrast, both cyclones and anticyclones appeared

to have less O_2 than expected based on nutrient concentrations in the layer below the DCM.

3. Particle-associated biomineral fluxes of PSi and PIC were inversely related to SLA_{corr} despite no differences in export of POC, PN, and PPO_4^{3-}. Elevated biomineral export at low SLA_{corr} presumably reflects increased contributions from silicifying and calcifying plankton consistent with observations of elevated biomass of Bacillaryophyceae and Prymnesiophytes in the cyclone DCM. Moreover, the $\delta^{15}N$ of sinking particles revealed differences in N sources supporting production across adjacent eddies, with a larger contribution by N_2 fixation in the anticyclone.

Our study highlights the spatiotemporal complexity of ocean ecosystems, and the inherent challenges such complexity presents to Eulerian observations such as the HOT program. Across a region of the ocean stretching a few hundreds of kilometers, the presence of strong, mature, mesoscale eddies of opposite polarity resulted in striking differences in ocean biogeochemistry. We found eddy-dependent isopycnal displacements through the upper ocean light field alter the steepness of the nutricline, influence the biomass of eukaryotic phytoplankton (including members of the prymnesiophytes and diatoms) and *Prochlorococcus*, and impact the export of opal and carbonate. These observations expand our understanding of the biogeochemical impacts of mesoscale motions by describing the stoichiometry of the erosion of the nutricline in cyclonic eddies and by highlighting a series of cascading dynamics that result from this erosion.

Acknowledgements

We warmly thank Tara Clemente (University of Hawaii) for her leadership during the HOE-Legacy 4 and MESO-SCOPE expeditions. We are also grateful to Tim Burrell, Eric Shimabukuro, and Ryan Tabata (University of Hawaii) for their tireless efforts during field operations. We are grateful to Joshua Weitz and David Demory (Georgia Institute of Technology) for their thoughtful comments on the manuscript. We thank Susan Curless, Eric Grabowski, and Alexa Nelson (University of Hawaii) for the analysis of inorganic nutrients and sinking particle fluxes. The isotopic composition of nitrogen of sinking particles was done by the Popp lab (University of Hawaii). SLA is available from the Copernicus Marine and Environment Monitoring Service (http://www.marine.copernicus.eu). HOT observations are available through HOT-DOGS (http://hahana.soest.hawaii.edu/hot/hot-dogs/). Results from the numerical model can be accessed at https://doi.org/10.6075/J0BR8QJ1. All other measurements used for the analyses of this manuscript are available at https://doi.org/10.5281/zenodo.5048504. This work was supported by grants from the Simons Foundation (# 329108 to DMK, EFD, MJF, MJC, AEW, SGJ; 721252 to DMK; 721223 to EFD; 721221 to MJC; 721256 to AEW; 721250 to SGJ).

References

Abell, J., Emerson, S., and Keil, R. G. (2005). Using preformed nitrate to infer decadal changes in DOM remineralization in the subtropical North Pacific. *Global biogeochemical cycles*, *19*(1). https://doi.org/10.1029/2004GB002285

Anderson, G. C. (1969). Subsurface chlorophyll maximum in the Northeast Pacific Ocean.

Limnology and Oceanography, 14, 386–391. https://doi.org/10.4319/lo.1969.14.3.0386

Anderson, L. A., and Sarmiento, J. L. (1994). Redfield ratios of remineralization determined by nutrient data analysis, *Global Biogeochemical Cycles*, 8(1), 65– 80. https://doi.org/10.1029/93GB03318

Anderson, L. A. (1995). On the hydrogen and oxygen content of marine phytoplankton. *Deep-Sea Research Part I: Oceanographic Research Papers*, 42, 1675–1680. https://doi.org/10.1016/0967-0637(95)00072-E

Ascani, F., Richards, K. J., Firing, E., Grant, S., Johnson, K. S., Jia, Y., ... and Karl, D. M. (2013). Physical and biological controls of nitrate concentrations in the upper subtropical North Pacific Ocean. *Deep-Sea Research Part II: Topical Studies in Oceanography*, *93*, 119-134. https://doi.org/10.1016/j.dsr2.2013.01.034

Bahamón, N., Velasquez, Z., and Cruzado, A. (2003). Chlorophyll *a* and nitrogen flux in the tropical North Atlantic Ocean. *Deep-Sea Research Part I: Oceanographic Research Papers*, 50(10–11), 1189–1203. https://doi.org/10.1016/S0967-0637(03)00145-6

Barone, B., Coenen, A. R., Beckett, S. J., McGillicuddy, D. J., Weitz, J. S., and Karl, D. M. (2019). The ecological and biogeochemical state of the North Pacific Subtropical Gyre is linked to sea surface height. *Journal of Marine Research*, *77*(2), 215-245. https://doi.org/10.1357/002224019828474241

Benitez-Nelson, C. R., Bidigare, R. R., Dickey, T. D., Landry, M. R., Leonard, C. L., Brown, S.

L., ... and Yang, E. J. (2007). Mesoscale eddies drive increased silica export in the subtropical Pacific Ocean. *Science* 316(5827), 1017-1021. https://doi.org/10.1126/science.1136221

Bidigare, R. R., Benitez-Nelson, C., Leonard, C. L., Quay, P. D., Parsons, M. L., Foley, D. G., and Seki, M. P. (2003). Influence of a cyclonic eddy on microheterotroph biomass and carbon export in the lee of Hawaii. *Geophysical Research Letters*, *30*(6). https://doi.org/10.1029/2002GL016393

Böttjer, D., Dore, J. E., Karl, D. M., Letelier, R. M., Mahaffey, C., Wilson, S. T., Zehr, J. P., and Church, M. J. (2016). Temporal variability of nitrogen fixation and particulate nitrogen export at Station ALOHA. *Limnology and Oceanography*, 62(1), 200-216. https://doi.org/10.1002/lno.10386

Brzezinski, M. A., and Nelson, D. M. (1989). Seasonal changes in the silicon cycle within a Gulf Stream warm-core ring. *Deep-Sea Research Part A. Oceanographic Research Papers*, 36(7), 1009-1030. https://doi.org/10.1016/0198-0149(89)90075-7

Carpenter, J. H. (1965). The accuracy of the Winkler method for dissolved oxygen analysis. *Limnology and Oceanography*, 10(1), 135-140. https://doi.org/10.4319/lo.1965.10.1.0135

Casciotti, K. L., Trull, T. W., Glover, D. M., & Davies, D. (2008). Constraints on nitrogen cycling at the subtropical North Pacific Station ALOHA from isotopic measurements of nitrate and particulate nitrogen. *Deep-Sea Research Part II: Topical Studies in Oceanography*, *55*(14-

15), 1661-1672. https://doi.org/10.1016/j.dsr2.2008.04.017

Chelton, D. B., Schlax, M. G., Samelson, R. M., and de Szoeke, R. A. (2007). Global observations of large oceanic eddies. *Geophysical Research Letters*, *34*(15). https://doi.org/10.1029/2007GL030812

Chelton, D. B., Gaube, P., Schlax, M. G., Early, J. J., and Samelson, R. M. (2011). The influence of nonlinear mesoscale eddies on near-surface oceanic chlorophyll. *Science*, 334, 328–332. https://doi.org/10.1126/science.1208897

Church, M. J., Mahaffey, C., Letelier, R. M., Lukas, R., Zehr, J. P., and Karl, D. M. (2009). Physical forcing of nitrogen fixation and diazotroph community structure in the North Pacific subtropical gyre. *Global Biogeochemical Cycles*, 23. https://doi.org/10.1029/2008GB003418

Cullen, J. J. (2015). Subsurface chlorophyll maximum layers: enduring enigma or mystery solved?. *Annual Review of Marine Science*, 7, 207–239. https://doi.org/10.1146/annurev-marine-010213-135111

Cullen, J. J., and Eppley, R. W. (1981). Chlorophyll maximum layers of the Southern California Bight and possible mechanisms of their formation and maintenance. *Oceanologica Acta*, 4(1), 23–32.

Davis, C. S., and McGillicuddy, D. J. (2006). Transatlantic abundance of the N2-fixing colonial

cyanobacterium Trichodesmium. *Science*, *312*(5779), 1517-1520. https://doi.org/10.1126/science.1123570

Dore, J. E., Houlihan, T., Hebel, D. V., Tien, G., Tupas, L., and Karl, D. M. (1996). Freezing as a method of sample preservation for the analysis of dissolved inorganic nutrients in seawater. *Marine Chemistry*, 541; 53. https://doi.org/10.1016/0304-4203(96)00004-7.

Dore, J. E., Brum, J. R., Tupas, L. M., and Karl, D. M. (2002). Seasonal and interannual variability in sources of nitrogen supporting export in the oligotrophic subtropical North Pacific Ocean. *Limnology and Oceanography*, *47*(6), 1595-1607. https://doi.org/10.4319/lo.2002.47.6.1595

Dugenne, M., Henderikx Freitas, F., Wilson, S. T., Karl, D. M., and White, A. E. (2020). Life and death of *Crocosphaera* sp. in the Pacific Ocean: Fine scale predator–prey dynamics. *Limnology and Oceanography*, 65, 2603–2617. https://doi.org/10.1002/lno.11473

Dutkiewicz, S., Hickman, A. E., Jahn, O., Gregg, W. W., Mouw, C. B., and Follows, M. J. (2015). Capturing optically important constituents and properties in a marine biogeochemical and ecosystem model. *Biogeosciences*, 12, 4447–4481. https://doi.org/10.5194/bg-12-4447-2015

Emerson, S., and Hayward, T. L. (1995). Chemical tracers of biological processes in shallow waters of North Pacific: preformed nitrate distributions. *Journal of Marine Research*, 53(3), 499-513, https://doi.org/10.1357/0022240953213179

Falkowski, P. G., Ziemann, D., Kolber, Z., and Bienfang, P. K. (1991). Role of eddy pumping in enhancing primary production in the ocean. *Nature*, *352*(6330), 55-58. https://doi.org/10.1038/352055a0

Fawcett, S. E., Johnson, K. S., Riser, S. C., Van Oostende, N., and Sigman, D. M. (2018). Low-nutrient organic matter in the Sargasso Sea thermocline: A hypothesis for its role, identity, and carbon cycle implications. *Marine Chemistry*, 207: 108-123. https://doi.org/10.1016/j.marchem.2018.10.008

Fong, A. A., Karl, D. M., Lukas, R., Letelier, R. M., Zehr, J. P., & Church, M. J. (2008). Nitrogen fixation in an anticyclonic eddy in the oligotrophic North Pacific Ocean. *The ISME journal*, *2*(6), 663-676. https://doi.org/10.1038/ismej.2008.22

Foreman, R. K., Segura-Noguera, M., and Karl, D. M. (2016). Validation of Ti(III) as a reducing agent in the chemiluminescent determination of nitrate and nitrite in seawater. *Marine Chemistry*, 186: 83-9. https://doi.org/10.1016/j.marchem.2016.08.003

Gaube, P., D. J. McGillicuddy, D. B. Chelton, M. J. Behrenfeld, and P. G. Strutton, (2014). Regional variations in the influence of mesoscale eddies on near-surface chlorophyll, *Journal of Geophysical Research: Oceans*, 119, 8195–8220. https://doi.org/10.1002/2014JC010111

Goldman, J. C. (1993). Potential role of large oceanic diatoms in new primary production. *Deep-*

Sea Research Part I: Oceanographic Research Papers, 40(1), 159-168. https://doi.org/10.1016/0967-0637(93)90059-C

Goldman, J.C., and McGillicuddy, D. Jr J. (2003). Effect of large marine diatoms growing at low light on episodic new production. *Limnology and Oceanography*, 48, 1176-1182. https://doi.org/10.4319/lo.2003.48.3.1176

Grabowski, E., Letelier, R. M., Laws, E. A., and Karl, D. M. (2019). Coupling carbon and energy fluxes in the North Pacific Subtropical Gyre. *Nature Communications*, 10(1), 1-9. https://doi.org/10.1038/s41467-019-09772-z

Guo, M., Xiu, P., Chai, F., and Xue, H. (2019). Mesoscale and submesoscale contributions to high sea surface chlorophyll in subtropical gyres, *Geophysical Research Letters*, 46(22), 13217-13226. https://doi.org/10.1029/2019GL085278

Herbland, A., and Voituriez, B. (1979). Hydrological structure analysis for estimating the primary production in the tropical Atlantic Ocean. *Journal of Marine Research*, 37(1), 87–101.

Hogle, S. L., Dupont, C. L., Hopkinson, B. M., King, A. L., Buck, K. N., Roe, K. L., Stuart, R. K., Allen, A. E., Mann, E. L., Johnson, Z. I., and Barbeau, K. A (2018). Pervasive iron limitation at subsurface chlorophyll maxima of the California Current. *Proceedings of the National Academy of Sciences*, 115(52), 13300-13305. https://doi.org/10.1073/pnas.1813192115

Johnson, K. S., Riser, S. C., and Karl, D. M. (2010). Nitrate supply from deep to near-surface waters of the North Pacific subtropical gyre. *Nature*, 465(7301), 1062-1065. https://doi.org/10.1038/nature09170

Karl, D. M., Bidigare, R. R., and Letelier, R. M. (2001). Long-term changes in plankton community structure and productivity in the North Pacific Subtropical Gyre: The domain shift hypothesis, *Deep-Sea Research Part II: Topical Studies in Oceanography*, 48, 1449–1470. https://doi.org/10.1016/S0967-0645(00)00149-1

Karl, D. M., Christian, J. R., Dore, J. E., Hebel, D. V., Letelier, R. M., Tupas, L. M., and Winn, C. D. (1996). Seasonal and interannual variability in primary production and particle flux at Station ALOHA. *Deep-Sea Research Part II: Topical Studies in Oceanography*, 43(2-3), 539-568. https://doi.org/10.1016/0967-0645(96)00002-1

Karl, D. M. (1999). A sea of change: biogeochemical variability in the North Pacific Subtropical Gyre. *Ecosystems*, 2(3), 181-214. https://doi.org/10.1007/s100219900068

Karl, D., Letelier, R., Tupas, L., Dore, J., Christian, J., and Hebel, D. (1997). The role of nitrogen fixation in biogeochemical cycling in the subtropical North Pacific Ocean. *Nature*, *388*(6642), 533-538. https://doi.org/10.1038/41474

Knauer, G. A., Martin, J. H., and Bruland, K. W. (1979). Fluxes of particulate carbon, nitrogen, and phosphorus in the upper water column of the northeast Pacific. *Deep-Sea Research Part A.*

Oceanographic Research Papers, 26(1), 97-108. https://doi.org/10.1016/0198-0149(79)90089-X

Kuwahara, V. S., Nencioli, F., Dickey, T. D., Rii, Y. M., and Bidigare, R. R. (2008). Physical dynamics and biological implications of Cyclone Noah in the lee of Hawai'i during E-Flux I. *Deep-Sea Research Part II: Topical Studies in Oceanography,* 55, 1231-1251. https://doi.org/10.1016/j.dsr2.2008.01.007

Letelier, R. M., Karl, D. M., Abbott, M. R., Flament, P., Freilich, M., Lukas, R., and Strub, T. (2000). Role of late winter mesoscale events in the biogeochemical variability of the upper water column of the North Pacific Subtropical Gyre. *Journal of Geophysical Research: Oceans*, 105, 28723–39. https://doi.org/10.1029/1999JC000306

Letelier, R. M., Karl, D. M., Abbott, M. R., & Bidigare, R. R. (2004). Light driven seasonal patterns of chlorophyll and nitrate in the lower euphotic zone of the North Pacific Subtropical Gyre. *Limnology and Oceanography*, 49, 508–519. https://doi.org/10.4319/lo.2004.49.2.0508

Letscher, R. T., and Villareal, T. A. (2018). Evaluation of the seasonal formation of subsurface negative preformed nitrate anomalies in the subtropical North Pacific and North Atlantic. *Biogeosciences*, 15(21), 6461-6480. https://doi.org/10.5194/bg-15-6461-2018

Lewis, M. R., Hebert, D., Harrison, W. G., Platt, T., and Oakey, N. S. (1986). Vertical nitrate fluxes in the oligotrophic ocean. *Science*, 234(4778), 870–873. https://doi.org/10.1126/science.234.4778.870

Li, B., Karl, D. M., Letelier, R. M., and Church, M. J. (2011). Size-dependent photosynthetic variability in the North Pacific Subtropical Gyre. *Marine Ecology Progress Series*, 440, 27–40. https://doi.org/10.3354/meps09345

Li, B., Karl, D. M., Letelier, R. M., Bidigare, R. R., and Church, M. J. (2013). Variability of chromophytic phytoplankton in the North Pacific Subtropical Gyre. *Deep-Sea Research Part II: Topical Studies in Oceanography*, *93*, 84-95. https://doi.org/10.1016/j.dsr2.2013.03.007

Mackas, D. L., Denman, K. L., and Abbott, M. R. (1985). Plankton patchiness: biology in the physical vernacular. *Bulletin of Marine Science*, 37(2), 652-674.

Malmstrom, R. R., Coe, A., Kettler, G. C., Martiny, A. C., Frias-Lopez, J., Zinser, E. R., and Chisholm, S. W. (2010). Temporal dynamics of *Prochlorococcus* ecotypes in the Atlantic and Pacific oceans. *The ISME journal*, 4, 1252–64. https://doi.org/10.1038/ismej.2010.60

Marshall, J., Hill, C., Perelman, L., and Adcroft, A. (1997). Hydrostatic, quasi-hydrostatic, and nonhydrostatic ocean modeling. *Journal of Geophysical Research: Oceans*, 102, 5733–5752. https://doi.org/10.1029/96JC02776

McClain, C. R., Signorini, S. R., and Christian, J. R. (2004). Subtropical gyre variability observed by ocean-color satellites. *Deep Sea Research Part II: Topical Studies in Oceanography*, 51(1-3), 281-301. https://doi.org/10.1016/j.dsr2.2003.08.002

McGillicuddy Jr, D. J., Johnson, R. J., Siegel, D. A., Michaels, A. F., Bates, N., and Knap, A. H. (1999). Mesoscale variations of biogeochemical properties in the Sargasso Sea. *Journal of Geophysical Research: Oceans,* 104, 13381-13394. https://doi.org/10.1029/1999JC900021

McGillicuddy Jr, D. J., and Robinson, A. R. (1997). Eddy-induced nutrient supply and new production in the Sargasso Sea. *Deep-Sea Research Part I: Oceanographic Research Papers*, 44, 1427–1450. https://doi.org/10.1016/S0967-0637(97)00024-1

Menden-Deuer, S., and Lessard, E. J. (2000). Carbon to volume relationships for dinoflagellates, diatoms, and other protist plankton. *Limnology and Oceanography* 45, 569-579. https://doi.org/10.4319/lo.2000.45.3.0569

Munk, W. (2002). The evolution of physical oceanography in the last hundred years. *Oceanography*, *15*(1), 135-142. https://doi.org/10.5670/oceanog.2002.45

Pedlosky, J. (1990). The dynamics of the oceanic subtropical gyres. *Science*, 248(4953), 316-322. https://doi.org/10.1126/science.248.4953.316

Raven, J. A., and Crawfurd, K. (2012). Environmental controls on coccolithophore calcification. *Marine Ecology Progress Series*, 470, 137-166. https://doi.org/10.3354/meps09993

Redfield, A. C. (1958). The biological control of chemical factors in the environment. *American*

scientist, *46*(3), 205-222.

Rii, Y. M., Brown, S. L., Nencioli, F., Kuwahara, V., Dickey, T., Karl, D. M., and Bidigare, R. R. (2008).The transient oasis: Nutrient-phytoplankton dynamics and particle export in Hawaiian lee cyclones. *Deep-Sea Research Part II: Topical Studies in Oceanography*, 55(10–13), 1275–1290. https://doi.org/10.1016/j.dsr2.2008.01.013

Roesler, C., Uitz, J., Claustre, H., Boss, E., Xing, X., Organelli, E., ... and Barbieux, M. (2017). Recommendations for obtaining unbiased chlorophyll estimates from in situ chlorophyll fluorometers: A global analysis of WET Labs ECO sensors. *Limnology and Oceanography: Methods*, 15(6), 572–585. https://doi.org/10.1002/lom3.10185

Scharek, R., Latasa, M., Karl, D. M., and Bidigare, R. R. (1999). Temporal variations in diatom abundance and downward vertical flux in the oligotrophic North Pacific gyre. *Deep-Sea Research Part I: Oceanographic Research Papers*, 46(6), 1051-1075. https://doi.org/10.1016/S0967-0637(98)00102-2

Schlax, M. G., and Chelton, D. B. (2016). The "Growing Method" of Eddy Identification and Tracking in Two and Three Dimensions. *Corvallis: College of Earth, Ocean and Atmospheric Sciences, Oregon State University*.

Sosik, H. M., and Olson, R. J. (2007). Automated taxonomic classification of phytoplankton sampled with imaging in flow cytometry. *Limnology and Oceanography: Methods*, 5, 204-216.

https://doi.org/10.4319/lom.2007.5.204

Strickland, J. D. H., and Parsons, T. R. (1972). A practical handbook of seawater analysis. *Fisheries Research Board of Canada*, 2nd edition. https://doi.org/10.1002/iroh.19700550118

Sweeney, E. N., McGillicuddy Jr, D. J., and Buesseler, K. O. (2003). Biogeochemical impacts due to mesoscale eddy activity in the Sargasso Sea as measured at the Bermuda Atlantic Time-series Study (BATS). *Deep-Sea Research Part II: Topical Studies in Oceanography*, 50(22–26), 3017–3039. https://doi.org/10.1016/j.dsr2.2003.07.008

Vaillancourt, R. D., Marra, J., Seki, M. P., Parsons, M. L., and Bidigare, R. R. (2003). Impact of a cyclonic eddy on phytoplankton community structure and phytoplankton competency in the subtropical North Pacific Ocean. *Deep-Sea Research Part I: Oceanographic Research Papers*, 50, 829-847. https://doi.org/10.1016/S0967-0637(03)00059-1

Venrick, E. L. (1982). Phytoplankton in an oligotrophic ocean: observations and questions. *Ecological Monographs*, 52, 129–154. https://doi.org/10.2307/1942608

Venrick, E. L. (1990). Mesoscale patterns of chlorophyll *a* in the central North Pacific. *Deep-Sea Research Part A. Oceanographic Research Papers*, 37(6), 1017-1031. https://doi.org/10.1016/0198-0149(90)90108-8

Venrick, E. L. (1999). Phytoplankton species structure in the central North Pacific 1973-1996:

variability and persistence, *Journal of Plankton Research*, 21, 1029–1042. https://doi.org/10.1093/plankt/21.6.1029

Villareal, T., Altabet, M., and Culver-Rymsza, K. (1993). Nitrogen transport by vertically migrating diatom mats in the North Pacific Ocean. *Nature* **363,** 709–712. https://doi.org/10.1038/363709a0

Wilson, S., del Valle, D., Segura-Noguera, M., and Karl, D. (2014). A role for nitrite in the production of nitrous oxide in the lower euphotic zone of the oligotrophic North Pacific Ocean. *Deep-Sea Research Part I: Oceanographic Research Papers*, 85, 47-55. 10.1016/j.dsr.2013.11.008.

Wilson, S. T., Aylward, F. O., Ribalet, F., Barone, B., Casey, J. R., Connell, P. E., ... and DeLong, E. F. (2017). Coordinated regulation of growth, activity and transcription in natural populations of the unicellular nitrogen-fixing cyanobacterium *Crocosphaera*. *Nature Microbiology*, *2*(9), 1-9. https://doi.org/10.1038/nmicrobiol.2017.118

Wunsch, C. (1997). The vertical partition of oceanic horizontal kinetic energy. *Journal of Physical Oceanography*, 27, 1770–1794. https://doi.org/10.1175/1520-0485(1997)027<1770:TVPOOH>2.0.CO;2